

Constraining star formation rates in cool-core brightest cluster galaxies

Rupal Mittal^{1,2}, John T. Whelan^{1,3}, Françoise Combes⁴

¹ *Max-Planck-Institut für Gravitationsphysik (Albert-Einstein-Institut), D-30167 Hannover, Germany*

² *Chester F. Carlson Center for Imaging Science, Rochester Institute of Technology, Rochester, NY 14623, USA*

³ *School of Mathematical Sciences, Rochester Institute of Technology, Rochester, NY 14623, USA*

⁴ *Observatoire de Paris, LERMA, CNRS, 61 Av. de l'Observatoire, 75014 Paris, France*

Received/Accepted

ABSTRACT

We used broad-band imaging data for 10 cool-core brightest cluster galaxies (BCGs) and conducted a Bayesian analysis using stellar population synthesis to determine the likely properties of the constituent stellar populations. Determination of ongoing star formation rates (SFRs), in particular, has a direct impact on our understanding of the cooling of the intra-cluster medium (ICM), star formation and AGN-regulated feedback. Our model consists of an old stellar population and a series of young stellar components. We calculated marginalized posterior probability distributions for various model parameters and obtained 68 % plausible intervals from them. The 68 % plausible interval on the SFRs is broad, owing to a wide range of models that are capable of fitting the data, which also explains the wide dispersion in the star formation rates available in the literature. The ranges of possible SFRs are robust and highlight the strength in such a Bayesian analysis.

The SFRs are correlated with the X-ray mass deposition rates (the former are factors of 4 to 50 lower than the latter), implying a picture where the cooling of the ICM is a contributing factor to star formation in cool-core BCGs. We find that 9 out of 10 BCGs have been experiencing starbursts since 6 Gyr ago. While four out of 9 BCGs seem to require continuous SFRs, 5 out of 9 seem to require periodic star formation on intervals ranging from 20 Myr to 200 Myr. This time scale is similar to the cooling-time of the ICM in the central (< 5 kpc) regions.

1 INTRODUCTION

Brightest cluster galaxies (BCGs) are luminous early-type galaxies found at the centers of rich galaxy clusters. These are unique not only in their special location but also in that they occupy the most massive end of the galaxy luminosity function. In the hierarchical model of structure formation, the most massive objects form last – referred to as the bottom-up growth of structures.

An important consideration in the hierarchical models is the inclusion of AGN feedback, which ensures dry mergers, and in the absence of which, simulations irrevocably produce more luminous elliptical galaxies than observed and higher star formation rates (SFRs) than measured (e.g. Benson et al. 2003; Croton et al. 2005, 2006; Scannapieco et al. 2005; Kormendy et al. 2009). AGN feedback is also a viable solution to the cooling-flow problem in the centers of galaxy clusters. Numerous results have indeed confirmed that (a) radio-loud AGN dwell preferentially in BCGs, compared to other galaxies of the same stellar mass (von der Linden et al. 2007; Best et al. 2007; Bagchi & Kapahi 1994; Valentijn & Bijleveld 1983) and (b) cool-core clusters are particularly conducive for cD galaxies which have an AGN visible at radio wavelengths (e.g. Burns 1990; Birzan et al. 2004; Birzan et al. 2008; Mittal et al. 2009).

Due to the early formation of the stellar component in massive early-type galaxies, ellipticals are usually considered to be “red and dead” and are not expected to show any recent star formation. However, there is compelling observational evidence that is suggestive of slow but gradual star formation in ellipticals within the last 1 Gyr. Kaviraj et al. (2007b), for example, examined 2100 early-type galaxies using SDSS and GALEX photometry data and found that at least 30% of the galaxies have experienced recent star formation (within 1 Gyr), contributing 1% to 3% to the total stellar mass. Similarly, Pipino & Matteucci (2004) and Liu et al. (2012) studied samples of 7 and 120 early-type BCGs, respectively, and found a recent starburst superimposed on an old stellar component for all of them.

BCGs at the centers of cooling flows are a special category of massive ellipticals. Rafferty et al. (2008) investigated the link between star formation, cooling of the intracluster gas and AGN feedback. They studied a sample of 47 BCGs in cool-core clusters and found that only those BCGs with gas cooling times < 0.8 Gyr show an increase in star formation towards galaxy centers. A number of studies have indeed found significant star formation in cool-core BCGs (e.g. Hansen et al. 1995; McNamara et al. 1989; Crawford et al. 1999; Mittaz et al. 2001; O’Dea et al. 2004; McNamara et al. 2004; Hicks & Mushotzky 2005; Rawle et al. 2012; Hoffer et al.

2012; Liu et al. 2012; Fraser-McKelvie et al. 2014) with the implication that the cool gas at the centers of cooling flows may be feeding the star formation in them. In some systems, it has been shown that AGN activity may well also trigger star formation in the central regions (e.g. O’Dea et al. 2004; Tremblay et al. 2012a). While the general consensus is that the AGN feedback is regulating the cooling flows, it remains largely unclear as to how the cooling time-scale relates to the AGN duty cycle and the time-scale of star formation.

In this work, we study the stellar populations of a sample of cool-core brightest cluster galaxies using broad-band imaging fluxes to fit the observed spectral energy distributions (SED) with the best-fit models obtained from stellar population synthesis (SPS). The study implements a Bayesian approach to compare the observed SEDs to models consisting of both old and young stellar populations to constrain a family of parameters. The cool-core BCGs are taken from a sample studied in an open time Herschel key programme in which, Herschel photometry and spectroscopy of 11 strong cool-core BCGs was conducted. The aim of the Herschel project included determining the dust temperatures and masses, and understanding the heating mechanisms of the ionized, molecular and atomic filaments that surround several of the cool-core BCGs. Note that the Herschel sample is not complete. It was chosen as to cover a wide range in X-ray, optical and radio luminosities so that correlations based on the physical properties of the BCGs could be examined. Results of this ongoing study can be found in Edge et al. (2010a), Edge et al. (2010b), Mittal et al. (2011) and Mittal et al. (2012).

One of the goals of the current study is to determine the ongoing star formation rates (SFRs) in the BCGs at the centers of strong cool-core clusters (SCC) – defined as those clusters for which the central gas cooling time is shorter than a Gyr (Mittal et al. 2009). This is of key importance to understand the factors leading to an order of magnitude discrepancy between the expected and observed rates of gas mass condensation in galaxy cluster cores. It is paramount that we understand the degeneracies among the physical properties parameterizing the stellar populations, in particular, the young stellar population, so that we may better understand its connection to the gas cooling out of the intracluster medium.

Within the framework of AGN-regulated feedback in cool-core clusters, it is commonly believed that the AGN outbursts are periodically heating up the in-falling cooling intracluster-gas (Fabian 1994; Peterson et al. 2003). Since it has been shown that the cool-core BCGs show enhanced level of star formation compared to other ellipticals of the same mass (e.g. Edwards et al. 2007; Wang et al. 2010), it is also believed that the star-formation activity may somehow be tied to the cooling of the ICM gas and the AGN-regulated heating (Rafferty et al. 2008; O’Dea et al. 2008; Donahue et al. 2010; Tremblay et al. 2012b,a). A rather ambitious goal of this study is to determine if there is any periodicity in the young stellar component in cool-core BCGs on a similar time-scale as the cooling time.

A crucial source of concern that provides a further motivation to conduct this study is a wide range of star formation rates available in the literature for a given BCG with rather small errorbars. An important question that we would like to be able to address is the accuracy with which we may estimate the star formation rates of BCGs from the data amidst a large subset of unknown model parameters.

The study utilizes HST (far-ultraviolet and optical), GALEX (near-ultraviolet and far-ultraviolet), SDSS (optical) and 2MASS (near-infrared) photometric data points to investigate the best-

fitting superposition of old and young synthetic stellar spectra. In Section 2 we describe the observations and the various data used in this work and in Section 3 we discuss the photometry analysis. In Section 4 we describe the common methods of determining star formation rates and in Section 5 we introduce the Bayesian technique of inferring stellar population parameters, including the star formation rates. In Section 6, we discuss the model parameters and in Section 7 we focus on some of the concerning issues. In Section 8 we present the results of the Bayesian inference technique using galaxy SEDs and SPS. In Section 9 we correlate the inferred SFRs with the cooling of the ICM and AGN heating and in Section 10 we give our conclusions. We assume throughout this paper the Λ CDM concordance Universe, with $H_0 = 71 h_{71} \text{ km s}^{-1} \text{ Mpc}^{-1}$, $\Omega_m = 0.27$ and $\Omega_\Lambda = 0.73$ (Larson et al. 2011; Jarosik et al. 2011).

2 DATA ACQUISITION AND DESCRIPTION

The Herschel sample contains 11 cool-core BCGs, all of which are located in the centers of clusters with the central gas cooling times shorter than 1 Gyr. The BCG of the Centaurus cluster of galaxies, which we studied in detail in Mittal et al. (2011), is the closest BCG in the Herschel sample with a redshift of 0.01016 (Postman & Lauer 1995). Owing to its proximity, we were unable to obtain an accurate estimate of the background in the Hubble data. Furthermore, it lacks SDSS data as well and so due to the lack of any reliable photometric constraints we were unable to study it. Some of the observational characteristics of the remaining 10 BCGs in the Herschel sample are given in Table 1 and displayed in Figures 1 and 2 are the optical and FUV image of the BCGs.

2.1 Hubble Data

The optical data for Hydra-A and RXC J1504 and the FUV data for PKS 0745-191, Hydra-A, A 1068, RXC J1504 and A 2199 were acquired as part of the HST Proposal 12220, “Linking Star Formation with Intracluster Medium Cooling and AGN Heating in a Sample of Herschel Galaxy Clusters” (PI: R. Mittal, 7 cycles). The rest of the optical and FUV data were downloaded from the HST archive. All the data (proprietary and public) were retrieved from the MAST Data Archiving Distribution System (DADS). The data were reduced through the standard On-The-Fly-Reprocessing pipeline, kindly provided by the Space Telescope Science Institute (STScI), which includes tasks such as, flat-fielding, dark-subtraction, bias-subtraction and non-linearity correction.

The native units of the final calibrated HST images are $\text{e}^- \text{ s}^{-1}$ (or counts s^{-1}), which were converted into $\text{erg s}^{-1} \text{ cm}^{-2} \text{ \AA}^{-1}$ using the header keyword, PHOTFLAM. PHOTFLAM is defined as the mean flux density of a source in $\text{erg s}^{-1} \text{ cm}^{-2} \text{ \AA}^{-1}$ that produces 1 count per second in the HST observing mode used for the observation.

2.1.1 HST Optical Data

The HST instruments used for the optical data were the Wide-Field Planetary Camera 2 (WFPC2) with a field of view of $2.5' \times 2.5'$ at a resolution of $0.1'' \text{ pix}^{-1}$, the Wide Field Channel (WFC) included in the Advanced Camera for Surveys (ACS) with a field of view of $3.4' \times 3.4'$ at a resolution of $0.05'' \text{ pix}^{-1}$ and the Wide Field Camera 3 (WFC3) with a field of view of $2.7' \times 2.7'$ at a resolution of $0.04'' \text{ pix}^{-1}$.

All observations involved either dithering (small shifts between successive exposures) or split exposures (CR-SPLIT) so as to

Table 1. Basic properties of the sample BCGs taken from NED. The 1.4 GHz radio luminosities have been compiled from literature (Birzan et al. 2004; Birzan et al. 2008; Mittal et al. 2009; Govoni et al. 2009, and NED).

Cluster	RA (J2000)	Dec (J2000)	Redshift	1'' (in kpc)	E(B-V)	$L_{\nu(1.4 \text{ GHz})}$ (in 10^{24} W/Hz)
NGC 1275	03h19m48.16s	+41d30m42.1s	0.01756	0.352	0.144	15.44 ± 0.46
PKS 0745-191	07h47m31.35s	-19d17m39.7s	0.10280	1.868	0.463	62.23 ± 2.21
Hydra-A	09h18m05.67s	-12d05m43.9s	0.05490	1.054	0.036	313.73 ± 2.78
ZwCl 3146	10h23m39.60s	+04d11m12.0s	0.28990	4.316	0.026	1.84 ± 0.26
A 1068	10h40m44.40s	+39d57m12.0s	0.13860	2.420	0.020	0.45 ± 0.05
A 1795	13h48m52.43s	+26d35m34.0s	0.06276	1.193	0.012	8.60 ± 0.28
A 1835	14h01m02.00s	+02d52m45.0s	0.25194	3.899	0.026	5.59 ± 0.18
RXC J1504	15h04m07.50s	-02d48m16.0s	0.21720	3.485	0.098	7.90 ± 0.24
A 2199	16h28m38.24s	+39d33m04.3s	0.03030	0.599	0.010	7.48 ± 0.21
A 2597	23h25m19.82s	-12d07m26.4s	0.08300	1.542	0.026	32.03 ± 1.01

facilitate the removal of cosmic ray events. Dithering has an added advantage over CR-SPLIT in that it also makes possible the removal of hot pixels and gaps between CCDs, hence, yielding better images. The WFC and WFC3 calibrated data had already been subjected to the cosmic-ray removal algorithm in the pipeline. This was not the case for the WFPC2 data. For the WFPC2 data, we extracted the single flat-fielded, dark-subtracted CR-SPLIT exposures and combined them using the IRAF task, MULTIDRIZZLE, with the cosmic-ray rejection tool switched on. MULTIDRIZZLE is a powerful tool with the ability to work on dither, mosaic and CR-SPLIT associations. Apart from masking cosmic-ray events, it calculates dithered offsets and field distortions (the latter being significant for ACS), which are then used to correctly register the individual exposures with respect to one another. The single exposures can be then drizzled onto separate output frames and later combined.

The WFC/F500M observations of Perseus were made with the aim of creating a mosaic of the BCG, NGC 1275 (PI: A. Fabian). The data comprised three pointings/visits (north-west, south-east and south-west), with two orbits per pointing and three-point dithering per observation. One of the two pointings for the north-west region had the incorrect World Coordinate System (WCS) associated with it (the reasons are not clear), which was fixed via cross-correlation of the images using the other pointing. The calibrated flat-fielded exposures were then combined using MULTIDRIZZLE. Even though MULTIDRIZZLE accurately calculates the dither offsets within a single visit, some residual offsets on the order of a few pixels may remain for multiple visits (which often entail guide star re-acquisitions). Small offsets, visible in the combined image of NGC 1275, were removed by cross-correlating overlapping stars and matching them using the IRAF tasks, DAOFIND and XYXYMATCH. The results from these tasks were fed into GEOMAP, which computes the geometric transformation between the individual exposures. The residual offsets determined this way were then used as an additional input to MULTIDRIZZLE.

2.1.2 HST Far-Ultraviolet Data

The far-ultraviolet (FUV) observations were made with the Solar Blind Channel (SBC) included in the ACS, which uses a Multi-Anode Microchannel Array detector, with a field of view of $34.6'' \times 30.8''$ at a resolution of $\sim 0.032'' \text{ pix}^{-1}$. Even though the ACS MAMA detector is not affected by cosmic rays, all observations included the dithering technique. This was primarily to eliminate hot and permanently damaged pixels, and to improve the PSF sampling.

The MAMA detector has no readout noise and very low detector noise, with the dark current rate of about $1.2 \times 10^{-5} \text{ e}^{-1} \text{ s}^{-1} \text{ pix}^{-1}$, making the dark correction unnecessary¹. The MAMA dark rate, though, fairly uniform at operating temperatures below 25 °C, increases with temperature which increases as the time elapses during observations. As has been noted in previous studies (e.g. O’Dea et al. 2004), this may also give rise to a secondary dark component in the form of a temperature-dependent glow near the upper-left quadrant of detector. We checked the detector temperatures for all observations listed in Table 2 and none of the recorded final temperatures go beyond 25 °C. Hence there was no need to apply any primary or secondary dark correction.

The SBC/F140LP observations of A 1795 had two pointings (north and south) separated by about $\sim 30''$. These were combined in a similar way as the WFC/F555M data for NGC 1275 using MULTIDRIZZLE.

2.2 Two Micron All Sky Survey (2MASS), Sloan Digital Sky Survey (SDSS) and Galaxy Evolutionary Explorer (GALEX) Data

In addition to the HST optical and FUV observations, we used broad-band data from Two Micron All Sky Survey (2MASS), Sloan Digital Sky Survey (SDSS) and Galaxy Evolutionary Explorer (GALEX) archives. In the following, we briefly describe the data acquisition and analysis.

The 2MASS is an all-sky survey conducted using the 1.3-m telescopes at Mt. Hopkins, USA, and CTIO, Chile, in three near-infrared bands – J-band ($1.25 \mu\text{m}$), H-band ($1.65 \mu\text{m}$) and K_s-band ($2.17 \mu\text{m}$) (2MASS Skrutskie et al. 2006). Since the number of galaxies in this study is small, we preferred to conduct our own photometry rather than rely on the catalog derivatives. We downloaded the images of our galaxies using the 2MASS Atlas image service. The pixel units in the Atlas images are “data-number” units, DN , which can be converted into magnitude using,

$$mag_{\text{vega}} = \text{MAGZP} - 2.5 \times \log 10(S) \quad (1)$$

where S is the background-subtracted flux in DN determined from integrating over the desired region and MAGZP is the zero-point magnitude available in the header of each retrieved image. Note the default 2MASS magnitudes refer to the Vega magnitude system. We used the conversions given in Blanton et al. (2005) to

¹ The dark correction has since recently been switched off in the standard ACS SBC pipeline.

Table 2. : HST Photometry Details. The columns indicate (1) cluster name, (2) instrument mode, (3) proposal ID, (4) the exposure time, (5) the pivot wavelength, (6) the photflam defined as the flux of the source that produces 1 count per sec, (7) the mean aperture radius (for elliptical apertures, the major and minor axes are given along with the angle of the major axis in brackets), (8) the mean Galactic-extinction corrected flux-density and (9) notes (“...” implies the measurement does not contain any or significant lines, “w lines” implies the measurement is contaminated by lines, “wo lines” implies the measurement has been corrected for the lines. For NGC 1275, “w AGN” implies the measurement contains AGN emission and “wo AGN” implies the measurement has been corrected for the AGN emission).

Cluster	Aperture/Filter	Prop ID	Exp. Time (s)	Wavelength (Å)	PHOTFLAM (erg s ⁻¹ cm ⁻² Å ⁻¹)	Aperture (arcsec)	Mean Flux Density (10 ⁻¹⁶ erg s ⁻¹ cm ⁻² Å ⁻¹)	Notes
NGC 1275	WFC/F550M	12132	12132	5581.5	3.848E-19	75	968.7	w AGN
		942.3	wo AGN
	WFC/F814W	12800	12900	7995.9	2.508E-20	75	827.3	w AGN
		811.1	wo AGN
PKS 0745-191	SBC/F140LP	12220	2715	1528.0	2.713E-17	3.5	17.9	...
	WFPC2/F814W	7337	2100	5439.0	3.439E-18	12 (5)	26.5	w lines
		25.0	wo lines
Hydra-A	SBC/F140LP	12220	2709	1528.0	2.713E-17	7.5	30.9	...
	WFC/F814W	12220	2367	8056.9	7.033E-20	23	73.5	...
ZwCl 3146	SBC/F165LP	11230	1170	1762.5	1.359E-16	8×4.5 (50)	4.9	...
	WFPC2/F606W	8301	1000	5996.8	1.888E-18	8.5×6.5 (50)	2.6	w lines
		2.5	wo lines
A 1068	SBC/F150LP	12220	2766	1612.2	4.392E-17	11×5.5 (61)	4.9	...
	WFPC2/F606W	8301	600	5996.8	1.888E-18	18.5×8.5 (40)	16.9	...
A 1795	†SBC/F140LP	11980	2394	1528.0	2.713E-17	12 + 18×8 (78)	25.4	...
	WFPC2/F555W	5212	1600	5442.9	3.483E-18	18×14.5 (95)	40.5	w lines
		40.2	wo lines
	WFPC2/F702W	5212	1600	6917.1	1.872E-18	26×22.5 (95)	63.9	w lines
		62.6	wo lines
A 1835	SBC/F165LP	11230	1170	1762.5	1.359E-16	5×4 (65)	6.8	...
	WFPC2/F702W	8249	7500	6917.1	1.872E-18	7×5 (65)	5.6	w lines
		5.4	wo lines
RXC J1504	SBC/F165LP	12220	2700	1762.5	1.360E-16	7.0	26.7	...
	WFC3/F689M	12220	2637	6876.3	3.714E-19	6.5	7.9	...
A 2199	SBC/F140LP	12220	2767	1528.0	2.713E-17	8.3×6.8 (95)	5.3	...
	WFC/F475W	12238	5370	4745.6	1.827E-19	50	283.0	...
	WFPC/F555W	7265	5200	5443.0	3.483E-18	47.8×35 (300)	292.6	...
	WFC/F814W	9293	700	8059.9	6.926E-20	75×47.5 (300)	367.3	...
A 2597	SBC/F150LP	11131	8141	1612.2	4.392E-17	10.5	14.9	...
	WFPC2/F450W	6228	2500	4557.3	9.022E-18	13×9 (55)	16.2	w lines
		14.8	wo lines
	WFPC2/F702W	6228	2100	6917.1	1.872E-18	20.5×10.5 (55)	23.6	w lines
		21.6	wo lines

obtain the AB magnitudes ($mag_{AB} = mag_{Vega} + C$, where $C = [0.91, 1.39, 1.85]$ for the J-, H- and K_s-bands, respectively), followed by the conversion,

$$mag_{AB} = -2.5 \times \log(F_\nu) - 48.60, \quad (2)$$

to obtain the flux, F_ν , in ergs s⁻¹ cm⁻² Hz⁻¹. Given a wavelength, λ , this can easily be converted into ergs s⁻¹ cm⁻² Å⁻¹.

The SDSS is an optical survey covering more than a quarter of the sky conducted using a 2.5-m telescope at Apache Point Observatory, USA, in five bands – ultraviolet or *u* (3543 Å), green or *g* (4470 Å), red or *r* (6231 Å) and near-infrared or *i* (7625 Å) and infrared or *z* (9135 Å) (York et al. 2000). We conducted our own aperture photometry. As the first step, we retrieved the “corrected” images using the tenth SDSS data release (Ahn et al. 2014). The “corrected” images are fully-calibrated, sky-subtracted images with

units of nanomaggies per pixel (1 nanomaggy = 3.631×10^{-6} Jansky). However, as noted by von der Linden et al. (2007); Bernardi et al. (2007); Lauer et al. (2007), the SDSS photometry for nearby BCGs is unreliable. These studies impute the reason to the level of sky background that has been over-estimated for large objects, especially in crowded fields, resulting in the luminosities of such objects to be under-estimated. Our strategy to overcome this problem comprised three steps a) we first de-calibrated the image (with the effect of converting nanomaggies to counts), b) we then obtained an interpolated sky image and added it to the de-calibrated image obtained in the first step and c) finally we re-calibrated the image. We sincerely thank Benjamin Alan Weaver from the SDSS help-desk for helping us obtain calibrated images of our BCGs with the sky included.

The GALEX is an ultraviolet imaging and spectroscopic

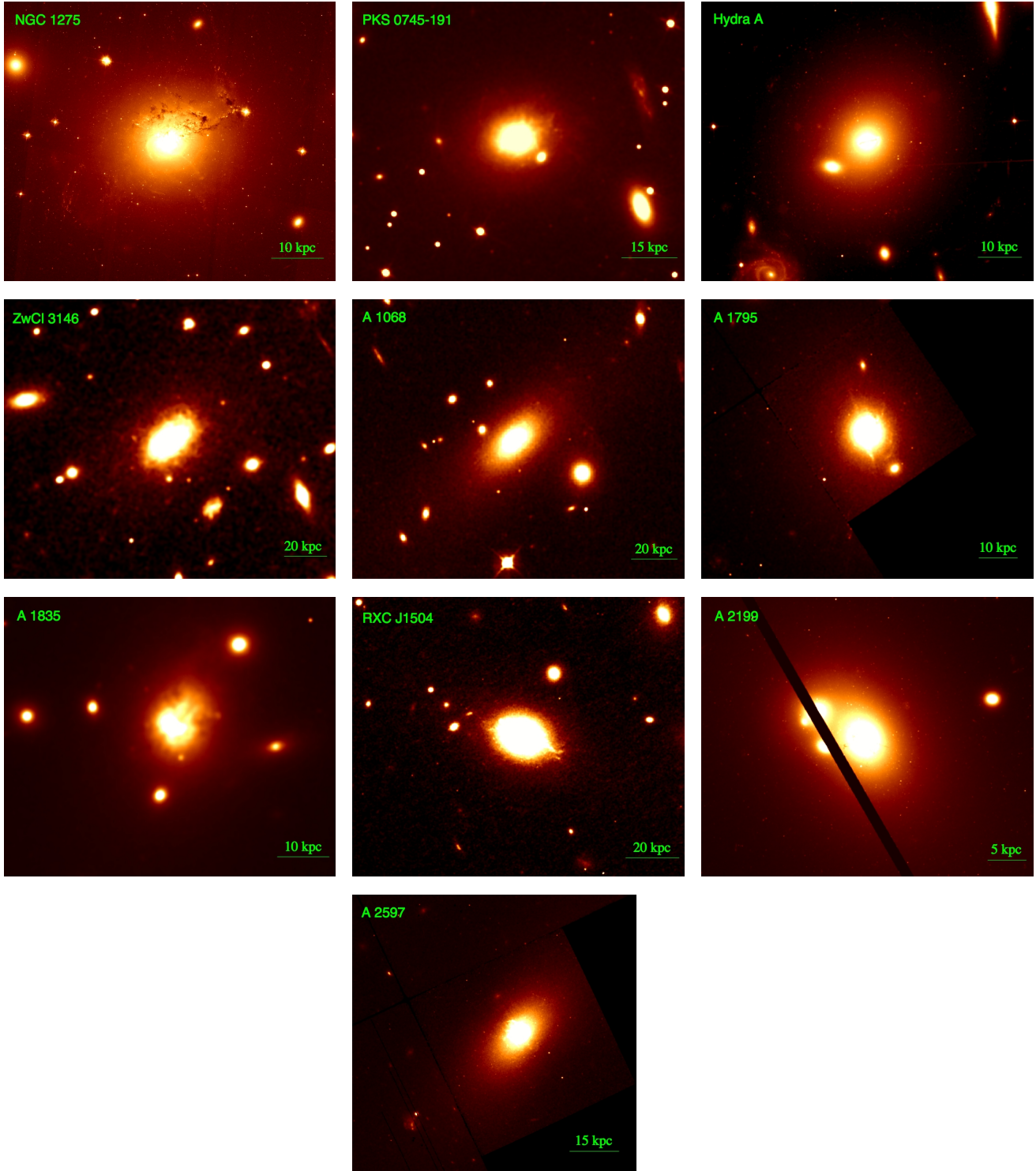


Figure 1. HST optical images of the BCGs.

survey of the sky conducted using a 0.5-m space-based telescope in two ultraviolet bands – far-ultraviolet (FUV) (1350-1780) Å and near-ultraviolet (NUV) (1770-2730) Å (Martin et al. 2005). We retrieved the images for all the galaxies in both the bands using GalexView. With the exception of PKS 0745-191 and A1068, we found data for all the BCGs. While PKS 0745-191 has no GALEX data, A1068 has only NUV data available. The images are in units of electrons

per second, which can be converted into $\text{ergs s}^{-1} \text{cm}^{-2} \text{\AA}^{-1}$ and AB magnitudes using the conversion factors given in http://galexgi.gsfc.nasa.gov/docs/galex/FAQ/counts_background.html.

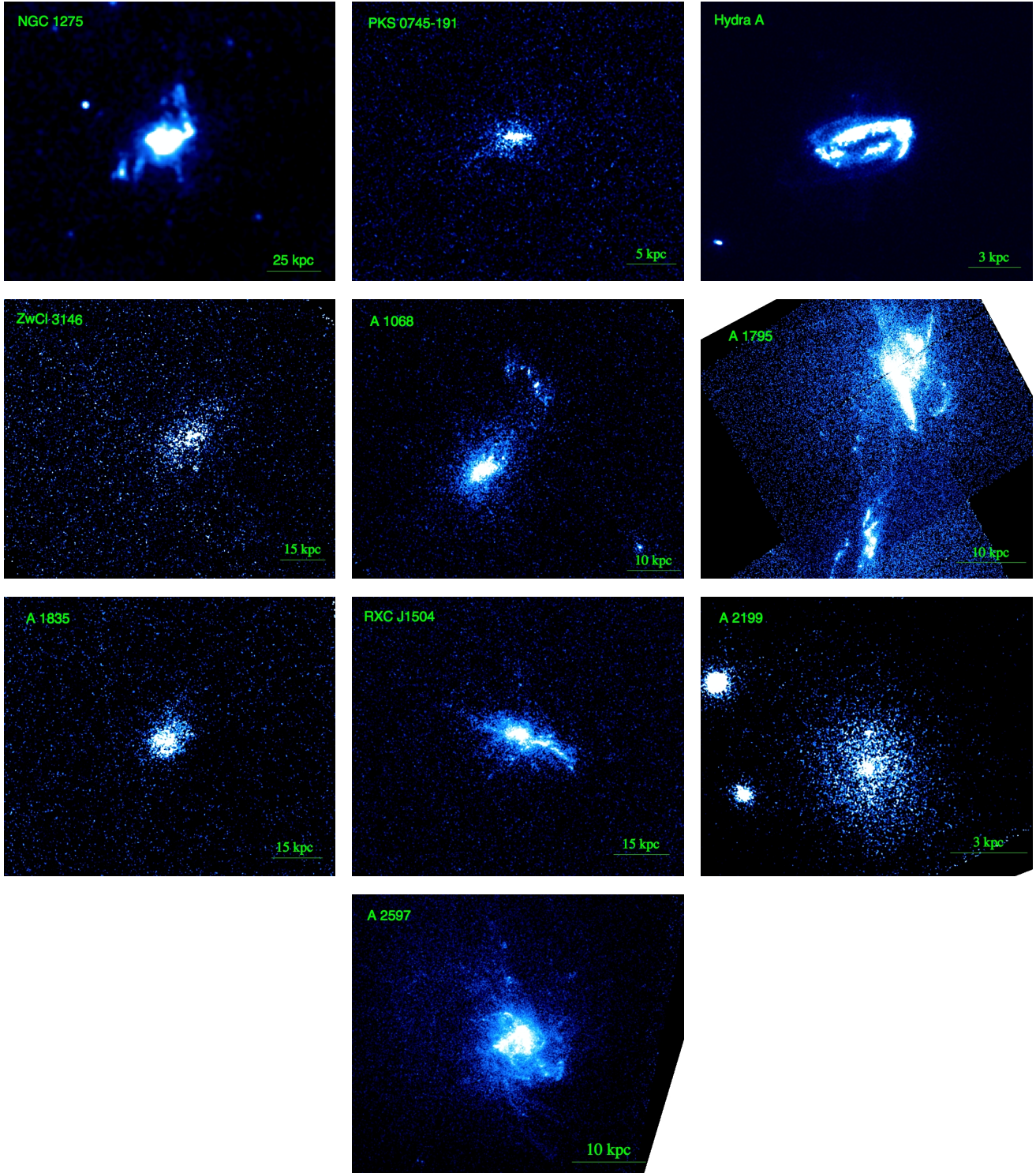


Figure 2. FUV images of the BCGs. NGC 1275 is from the *Galex* FUV detector and the others are from *HST* ACS/SBC FUV detector.

3 DATA ANALYSIS

3.1 Photometry

Here we describe the details of aperture photometry for the calculation of the UV, optical and infrared fluxes of the targets. We invoked a self-written code written in C programming language. We

used the `CFITSIO`² library of C routines for reading and writing FITS files and the `WSCTOOLS` package for reading the headers. The code involved placing an aperture (circular or elliptical) surrounding the emission from the BCG and integrating the flux over the aperture. Bright sources clearly not associated with the BCG but which lie

² <http://heasarc.gsfc.nasa.gov/fitsio/>

Table 3. : 2MASS Photometry Details. The columns indicate (1) cluster name, (2) the mean aperture radius in arcsec and (3) the mean Galactic-extinction corrected flux-density in units of 10^{-16} erg s $^{-1}$ cm $^{-2}$ Å $^{-1}$. For NGC 1275 the first row indicates the measurements with the AGN emission and the second row without.

Cluster	Aperture (arcsec)	Zero Point			Mean Flux Density		
		J	H	K	J	H	K
NGC 1275	69	20.9334	20.7121	20.0784	608.7	419.5	219.8
	599.2	412.5	214.5
PKS 0745-191	12	20.7320	20.3621	19.8461	22.5	13.7	7.4
Hydra-A	15	20.8561	20.4366	19.9282	42.0	30.4	15.2
ZwCl 3146	4	20.8114	20.4221	19.9039	1.9	1.6	0.8
A 1068	9×4.5 (40)	21.0129	20.3648	20.0921	8.4	5.8	3.7
A 1795	22	21.0392	20.3836	20.1139	39.0	28.8	18.0
A 1835	4.5	20.8215	20.3959	19.8729	4.0	2.7	2.0
RXC J1504	6.5	20.6326	20.3051	19.7951	4.3	3.6	2.1
A 2199	40×30 (300)	20.9123	20.6709	20.0397	211.3	147.9	74.8
A 2597	12	20.9755	20.4543	19.9394	15.0	10.6	6.4

Table 4. : SDSS Photometry Details. The columns indicate (1) cluster name, (2) the mean aperture radius in arcsec, (3) the mean Galactic-extinction corrected flux-density in units of 10^{-16} erg s $^{-1}$ cm $^{-2}$ Å $^{-1}$ and (4) notes (same as Table 2).

Cluster	Aperture (arcsec)	U	Mean Flux Density				Notes
			G	R	I	Z	
NGC 1275	75	907.6	688.7	w lines
		890.4	675.1	wo lines
ZwCl 3146	8×4.5 (5)	1.74	...	2.72	2.69	...	w lines
		1.74	...	2.68	2.69	...	wo lines
A 1068	12×6 (42)	3.7	12.8	...
A 1795	26×21 (110)	17.0	..	67.2	66.8	60.3	w lines
		17.0	...	66.7	64.8	60.3	wo lines
A 1835	7×5.5 (65)	3.61	...	6.12	5.88	5.59	w lines
		3.61	...	6.09	5.71	5.59	wo lines
RXC J1504	5	6.06	6.06	...
A 2199	47.5×30 (300)	...	267.1	...	336.4	318.4	...

within the source aperture were masked and the corresponding pixels were assigned the average flux of the neighbouring pixels.

The sky background was estimated and subtracted using the mean of the sky flux distribution. This was done by placing a circular aperture in a sky location devoid of visibly bright sources and making a histogram of the pixel flux values. At optical and infrared wavelengths, the sky distribution can be well described by a gaussian and so the average of the pixel values is the same as the mean of the gaussian. Adopting the mean as the statistic for sky background is useful in cases where there is a uniform distribution of bright pixels in areas close to the BCG since such bright pixels are expected to overlap also with the galaxy emission and so need to be subtracted from the integrated source flux in addition to the gaussian background. In some cases, where the background seemed to be non-uniform, we calculated the sky mean at more than one location and took the average of the values as the final flux.

The default photometric uncertainties used in this work cor-

respond to the absolute photometric calibration of the respective instruments. These are 10% for HST (Sirianni et al. 2005) and GALEX data, 7% for 2MASS data (Jarrett et al. 2000), 5% for SDSS u-band, and 3% for SDSS g-, r-, i- and z-band data³. The statistical uncertainties are usually very small. These were calculated using different techniques depending upon the observations. For example, for HST optical and ultraviolet observations, the root-mean-square of the background sky distribution was used. For GALEX observations, the poisson error was used. However, the errors so calculated vastly underestimate the uncertainty in the determined flux-densities. The main source of uncertainty arises from the choice of the aperture size. It is rather difficult to ascertain the amount of flux that is lost as the galaxy emission fades into noise. In order to obtain reliable estimates of the error-bars on the fluxes, we

³ <http://www.sdss.org/dr6/algorithms/fluxcal.html>

Table 5. : GALEX Photometry Details. The columns indicate (1) cluster name, (2) the exposure time, (3) the mean aperture radius in arcsec and (4) the mean Galactic-extinction corrected flux-density in units of 10^{-16} erg s $^{-1}$ cm $^{-2}$ Å $^{-1}$. While PKS 0745-191 has no GALEX data, a nearby galaxy in A2199 is not resolved from the BCG, and A1068 only has NUV data available. For NGC 1275 the first row indicates the measurements with the AGN emission and the second row without.

Cluster	Aperture (arcsec)	Mean Flux Density	
		FUV	NUV
NGC 1275	97.5	618.6	587.8
	...	447.1	458.1
Hydra-A	16.5	23.4	20.6
ZwCl 3146	12.5	12.4	3.5
A 1068	10	...	3.2
A 1795	30	26.5	17.5
A 1835	10.5	10.0	5.4
RXC J1504	13.5	44.9	13.5
A 2597	13.5	10.6	6.4

used several apertures (differing by up to 20% in size) and averaged the fluxes estimated therefrom. For some of the 2MASS and SDSS observations, the flux-uncertainties determined this way could be as large as 30% to 40%. For NGC 1275, the main source of uncertainty is the AGN emission that may be contributing to the total flux (see Section 7.3). In addition, NGC 1275 also includes a foreground high-velocity system (HVS, e.g. Burbidge & Burbidge 1965; Rubin et al. 1977; Hu et al. 1983). However, since the HVS covers only a small fraction of the northwest part of the BCG nebula, we have not subtracted its contribution from any of the flux-densities. Note there are no stellar or CO components detected (Salomé et al. 2006) from the HVS, and so its contribution to the star formation rate is likely to be small. Although Salomé et al. (2006) note that the absence of any stellar components may be due to the edge-on orientation of the disc, the HVS is undetected in the 2MASS maps as well.

Determining the total fluxes of brightest cluster galaxies is a very challenging task, especially since BCGs in cool-core galaxy clusters are often cD galaxies that are embedded in a pool of intracluster light (ICL, the origin of which is an issue of open debate), which in some cases can extend as far out as to a few hundreds of kiloparsecs (e.g. Lin & Mohr 2004). Albeit conservative, our approach aims to obtain reliable uncertainties on the estimated flux-densities of the galaxies in our sample. The details of aperture photometry are listed in Tables 2–5.

3.2 Galactic Extinction

The measured fluxes suffer from extinction, arising from dust in both the interstellar-medium of the Milky Way Galaxy (Galactic) and the BCG (internal). The internal extinction is included in the parameter set of the models described in Section 6. The Galactic extinction was corrected with the help of the mean extinction law of the form (Cardelli et al. 1989)

$$\langle A(\lambda)/A(V) \rangle = a(x) + b(x)/R_V. \quad (3)$$

Here, $A(\lambda)$ is the total extinction (in magnitude) at a given wavelength, λ , and $a(x)$ and $b(x)$ are wavelength-dependent coefficients which assume a polynomial form in $x = (1/\lambda) \mu\text{m}^{-1}$. $R_V = A(V)/E(B - V)$, where $E(B - V) = A(B) - A(V)$ is the selective extinction (in magnitude) in set bands, blue (B) and visual (V). The extinction law is a function of a single parameter, R_V , for which we adopt a value of 3.1, the standard value for the diffuse ISM (e.g. Schultz & Wiemer 1975; Sneden et al. 1978). The polynomial coefficients, $a(x)$ and $b(x)$, were taken from Cardelli et al. (1989), those appropriate for the optical ($1.1 \mu\text{m}^{-1} \leq x \leq 3.3 \mu\text{m}^{-1}$) and the ultraviolet ranges ($3.3 \mu\text{m}^{-1} \leq x \leq 8 \mu\text{m}^{-1}$). The Galactic $E(B - V)$ values were taken from the NASA/IPAC Extragalactic Database (NED⁴), and determined $A(\lambda)$ using Eqn. 3.

4 DETERMINING STAR FORMATION RATES: EXISTING METHODS

There are currently four main diagnostics of determining star formation rates in galaxies. The first method relies on measuring emission lines, predominantly, the optical H α line but often other recombination lines as well. The underlying assumption is that the emission lines originate from the ionized gas surrounding hot and young stars (30 M_\odot to 40 M_\odot) and, hence, serve as an instantaneous measure of the star formation rate (e.g. Kennicutt et al. 1994). This method probes only very recent star formation. The second method relies on the empirically suggested relation between the FUV–NUV colour and the logarithmic ratio of infrared to UV luminosity (also known as “IRX- β ” relation) (e.g. Meurer et al. 1999). However, this relation exhibits a good deal of scatter. The third method is to use the FUV luminosity (or sometimes the UV excess) directly together with synthetic stellar population models (e.g. Kennicutt 1998; O’Dea et al. 2004; Hicks & Mushotzky 2005; O’Dea et al. 2010; Mittal et al. 2011, 2012). This method, as we will describe below, does not work unless either the mass or the age of the young stellar population is known. For the latter two methods, one also assumes a certain initial mass function (IMF), describing the number density of stars as a function of mass, for the stellar populations. The fourth method is based on the far-infrared luminosity (8 μm to 1000 μm) originating from dust, assumed to be heated by young and hot stars.

A major drawback of the first three methods is that these are all subject to dust extinction. While Galactic extinction is accurately known for almost all lines of sight, the internal extinction arising due to dust in the host galaxies remains largely unknown. The fourth method, based on the FIR luminosity of the BCG, does not suffer from this drawback, but it is most suitable for dusty circumnuclear starbursts. For early-type galaxies, the FIR emission is not a very reliable indicator of young stars since the older stellar component may also contribute to the heating of dust. In addition, FIR emission is good calorimeter for measuring ionizing photons from young stars only if the dust opacity is high everywhere. Lastly, it may be that some of the IR emission detected is due to heating of dust by an AGN, and so it is important to use diagnostics such as the Spitzer IRAC 4.5/3.6 μm colour and [O III] $\lambda 5007/\text{H}\beta$ to identify the source of dust heating.

In this work, we use an alternative method to calculate the star formation rates that precludes many of the above shortcomings. This method is described in Section 5.1.

⁴ <http://nedwww.ipac.caltech.edu>

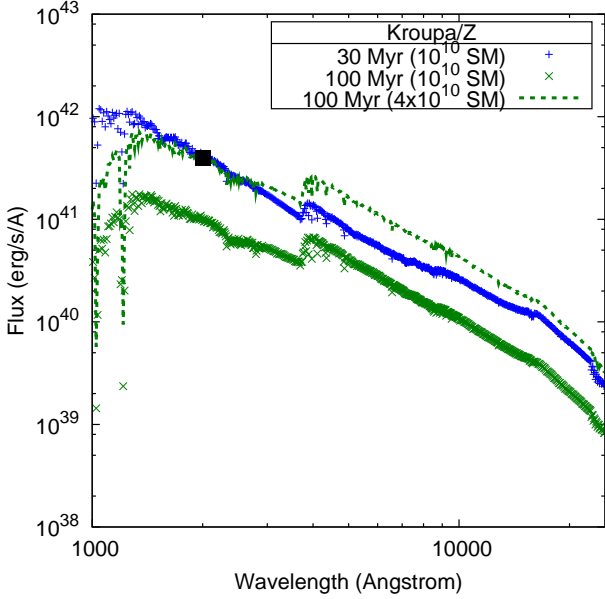


Figure 3. An aging stellar population. A 30 Myr stellar population can reproduce the observed FUV luminosity as easily as a 100 Myr stellar population four times as massive.

Mass-Age Degeneracy

FUV emission, in principle, is indicative of the presence of young and hot stars and so the FUV luminosity should be directly related to the active star formation. Synthesis stellar models using a grid of stellar evolution tracks from one of the well established spectral libraries can then be used to estimate the parameters of a stellar population in a galaxy. The simplest model is one where the initial mass function, metal abundance and internal extinction are known, which is usually not the case. Even so, that leaves two unknown parameters – the age and mass of the stellar population.

The situation may be understood by looking at Figure 3 which shows the spectral energy distribution (SED) created using starburst99 (Leitherer et al. 1999) with the IMF set to Kroupa and metallicity set to solar. We show the SED for a stellar population with a fixed mass of $10^{10} M_{\odot}$ at two different times during its evolution, 30 Myr (blue pluses) and 100 Myr (green crosses). It is clear that the overall normalization of the SED decreases as the stellar population ages. However, given the FUV luminosity (black filled square), it can either be fitted by a 30 Myr stellar population with a total mass of $10^{10} M_{\odot}$ or a 100 Myr stellar population but with a total mass of $4 \times 10^{10} M_{\odot}$, i.e. four times as massive. This is the mass-age degeneracy. Hence, several studies make use of colour instead of relying on a single data point. However, since we are interested in constraining a number of parameters (see Section 6), a well-sampled spectral energy distribution is needed that stretches across the entire electromagnetic spectrum from the FUV to IR. Under such circumstances, it is essential to fit both the young and old stellar population simultaneously.

5 DETERMINING STAR FORMATION RATES: BAYESIAN METHOD

5.1 Spectral Energy Distribution and Stellar Population Synthesis

In order to obtain the ongoing star formation rates and explore the star formation histories of BCGs, we make use of photometry conducted at several line-free wavebands covering a range from 1500 Å (FUV) and 25000 Å (IR). The FUV data were obtained from the *HST* telescope and *GALEX* (Martin et al. 2005), the NUV data (2300 Å) are taken from *GALEX* and the IR data (at three wavelengths) are all taken from the 2MASS survey (Skrutskie et al. 2006). We also used *HST* and *SDSS* data, where available. Note that since we are interested in the integrated galaxy emission, the different resolutions do not complicate handling of the data. For example, we compared the HST and GALEX FUV fluxes for BCGs for which both the data were available, and found no systematic differences despite a smaller point-spread function of the HST relative to GALEX. We have in total ≥ 8 data points for all BCGs except one (PKS 0745-191), which is lacking GALEX and SDSS data altogether, and for which there are 5 data points available.

Using the SEDs generated with the integrated flux-densities described above, we aim to fit the data with a model comprising two stellar populations: an old stellar population (OSP) and a young stellar population (YSP). Each of the two populations has at least two parameters – the age and the total mass. Assuming a stellar population that formed a certain time ago, the normalization of the SED scales linearly with the total mass in the stars. Hence, the flux-density at any given frequency, i , can be expressed in the form, $F_i(M, T) = M \times S_i(T)$, where M is the total mass and T is the age of the population. $S_i(T)$ is the flux-density per unit mass, which depends on the age. Our model consists of four more parameters, the IMF (Kroupa/Salpeter/Chabrier Salpeter 1955; Kroupa et al. 1993; Chabrier 2003), the metallicity ($0.4 Z_{\odot}$, Z , $2.5 Z_{\odot}$), the extinction law (Galactic/extra-Galactic) and the extinction, ($E(B - V) \in [0, 0.6]$). We represent the above four parameters along with the age of the OSP, τ_o , and YSP, τ_y , by θ . In view of the findings by Gao et al. (2004) and De Lucia & Blaizot (2007), we assume there exists a massive old stellar component at least as old as 11 Gyr (corresponding to a formation redshift of ~ 3). Hence, we carried out two sets of simulations in parallel. For one, we fixed the age of the OSP to a formation redshift of 3. For the other, the age of the OSP was left to vary over the range ~ 10 Gyr – 13 Gyr. The results of these simulations are described in Section 8. The modelled SEDs are convolved with the instrument bandpasses using the SYNPHOT library available within IRAF.

5.2 Statistical Method

We have a series of flux measurements $\{F_i\}$ with associated weights $\{w_i\}$, where $1/\sqrt{w_i}$ is the 1σ uncertainty associated with F_i . Given a family of models H parametrized by YSP mass M_y , OSP mass M_o , and some other (discretely-sampled) parameters θ , if the errors on the F_i are assumed to be independent and Gaussian, the likelihood function may be written as

$$P(\{F_i\}|M_o, M_y, \theta, H) = \sqrt{\prod_i \frac{w_i}{2\pi}} \exp\left(-\frac{\chi^2(M_o, M_y, \theta)}{2}\right) \quad (4)$$

where

$$\chi^2(M_o, M_y, \theta) = \sum_i w_i [F_i - M_o S_i^{(o)}(\theta) - M_y S_i^{(y)}(\theta)]^2, \quad (5)$$

where $S_i^{(o)}$ and $S_i^{(y)}$ are the flux per unit mass contributions from the OSP and YSP, respectively. The total observed flux at a given frequency, i , is assumed to be equal to

$$F_i^{(o)}(\theta) + F_i^{(y)}(\theta) = M_o S_i^{(o)}(\theta) + M_y S_i^{(y)}(\theta) \quad (6)$$

where $F_i^{(o)}$ and $F_i^{(y)}$ are the flux contributions from the OSP and YSP, respectively.

If we assume some prior probability distribution⁵ $P(M_o, M_y, \theta|H)$, Bayes's theorem allows us to construct a posterior probability distribution

$$P(M_o, M_y, \theta|\{F_i\}, H) = \frac{P(\{F_i\}|M_o, M_y, \theta, H)P(M_o, M_y, \theta|H)}{P(\{F_i\}|H)} \\ \propto P(M_o, M_y, \theta|H) \exp\left(-\frac{\chi^2(M_o, M_y, \theta)}{2}\right) \quad (7)$$

where we have absorbed everything not dependent on the parameters into a proportionality constant, which can be easily found from the requirement that the posterior be normalized, $\int dM_o \int dM_y \sum_{\theta} P(M_o, M_y, \theta|\{F_i\}, H) = 1$. To simplify both the approach and the calculations, we assume uniform priors, specifically uniform density in M_y and M_o , with the only restriction being $0 < M_y < M_o$, and that each of the discrete values of extinction, metallicity and τ_o , and the different possibilities for IMF and extinction law, are independently equally likely. Since we consider multiple-starburst models with N_{bursts} bursts evenly spaced in age from τ_y to $N_{\text{bursts}}\tau_y$ (see Section 6.4), we consider each of the discrete $(N_{\text{bursts}}, \tau_y)$ combinations sampled to have equal prior probability.

From the posterior probability, we can calculate useful probability distributions for various variables, marginalized over the others, such as the posterior probability density for the YSP mass

$$P(M_y|\{F_i\}, H) = \sum_{\theta} \int_{M_y}^{\infty} dM_o P(M_o, M_y, \theta|\{F_i\}, H) \quad (8)$$

or the OSP mass

$$P(M_o|\{F_i\}, H) = \sum_{\theta} \int_0^{M_o} dM_y P(M_o, M_y, \theta|\{F_i\}, H) \quad (9)$$

or the posterior probability distribution $P(x|\{F_i\}, H)$ for a discretely-sampled or categorical variable x which is among the parameters θ , whose value at some $x = x_0$ is

$$P(x_0|\{F_i\}, H) = \sum_{\theta: x=x_0} \int_0^{\infty} dM_o \int_0^{M_o} dM_y P(M_o, M_y, \theta|\{F_i\}, H) \quad (10)$$

By similar means, posterior probability densities can be constructed for derived quantities such as the mass ratio M_y/M_o and star formation rate⁶ $M_y/(N_{\text{bursts}}\tau_y)$. Because $\chi^2(M_o, M_y, \theta)$ is quadratic in M_o and M_y , the Gaussian integrals over those parameters in (8–10) can be done analytically, with the sums over the discrete values of the other parameters θ performed numerically. The number of simulations conducted for different values of the parameters, θ , varied from galaxy to galaxy, depending upon whether the HST FUV data was included or excluded, and whether the data contained lines or not. The minimum number of simulations for a given BCG was about 5×10^5 and the maximum was about 2×10^6 .

The SED-fitting method, like the other methods of estimating star formation rates, also faces severe challenges due to the existing

uncertainties in stellar evolution, dust properties and attenuation laws, IMFs and star formation histories (see Conroy et al. 2010, for an excellent review). However, as shown by Conroy et al. (2010); Pforr et al. (2012); Kaviraj et al. (2007b,a); Pipino & Matteucci (2004); Walcher et al. (2011), integrated light from galaxies at well-sampled points of the spectral energy distribution can be used to constrain the basic parameters, provided that marginalization techniques are used to incorporate the uncertainties in the model. The formulation described above does precisely that and we aspire to yield robust ranges of parameter values.

In principle, spectroscopic data in addition to photometric data are highly advantageous and reveal a lot more information about, for example, the age and metallicity of the various stellar populations. However, (a) photometric data are readily available for most of the BCGs whereas spectroscopic data are not and, more importantly, (b) recent studies claim a different from stellar origin for the H α filaments seen in cool-core BCGs (for e.g. Fabian et al. 2011; Ogrean et al. 2010). Many of the cool-core BCGs, including those being studied in this work, show signs of star formation, and so spectral lines such as [NII] $\lambda 6583$, H α , [OIII] $\lambda 5007$, H β and [OII] $\lambda 3727$ are expected from the photoionization of the surrounding gas. However, an unknown fraction of the intensity of the line emissions may have a non-stellar origin, such as reconnection diffusion that allows the hot intracluster gas to penetrate the cold filamentary gas (Fabian et al. 2011) or shock heating Ogrean et al. (2010), making usage of spectral lines problematic for modelling star formation, (c) spectroscopic data are usually available only for specific locations of the BCGs and so it is not possible to constrain their global stellar properties. In this work, therefore, we utilized only photometric data to constrain the age, mass and metallicity of both the old and young stellar populations, the initial mass function and the internal extinction.

There are several other SED-fitting libraries available, such as, STARLIGHT developed by Cid Fernandes et al. (2005), STECMAP developed by Ocvirk et al. (2006), VESPA developed by Tojeiro et al. (2007), ULYSS developed by Koleva et al. (2009), MOPED developed by Heavens et al. (2000) etc. However these are all spectral synthesis codes that make use of complete spectra of galaxies. Since these codes make use of a much larger dataset to obtain the model parameters, they may be able to better constrain certain stellar parameters by constraining them more tightly. But we are strongly inclined to using broadband SEDs for this work because of the reasons given above against using spectral emission lines and hence we devised our own code. The intention of this work is not to compete with the existing SED-fitting codes but rather to constrain the stellar populations of a special category of galaxies – cool-core BCGs. We designed our code to meet two main requirements: a) The fitting should include only broadband SEDs and b) the star formation history should include periodicity in star formation to test if there is a link between periodic cooling, star formation and AGN heating (Section 6.4).

6 STELLAR POPULATIONS: PARAMETERS

Now we will describe in detail the different ingredients of the models that we used to fit the SED of the BCGs. The various parameters and their range of variation is given in Table 6.

We used two publicly available codes for computing stellar population evolution synthesis models: STARBURST99 (Leitherer et al. 1999) and GALAXEV (Bruzual & Charlot 2003). While the former code was used primarily in order to construct simple stellar

⁵ This is a probability density in the continuous parameters M_o and M_y .

⁶ Since M_y is the total mass in the YSP, the mass in each starburst is M_y/N_{bursts} .

Table 6. The range of values for the final set of simulations. The star formation history included either single or multiple bursts. For the single burst model, the age of the YSP is varied between 0.5 Myr and 6 Gyr and for the multiple burst model, the age of the most recent burst is varied between 100 Myr to 1 Gyr, with the time interval between bursts set to the age of the most recent burst.

Parameter	Final Values
Old stellar population age, τ_o	11 Gyr (10 Gyr for ZwCl 3146 and 10.5 Gyr for A 1835)
Young stellar population age, τ_y	10 Myr to 6 Gyr
Initial Mass Function, IMF	Chabrier
Metallicity	$0.4Z_\odot, Z_\odot, 2.5Z_\odot$ ($Z_\odot - 0.4Z_\odot$ for NGC 1275 and PKS 0745-191)
Extinction laws	Galactic and extragalactic
Reddening, $E(B-V)$	0 - 0.6
Star Formation History, SFH	Instantaneous bursts

populations following the Salpeter and Kroupa initial mass functions, the latter was used to construct simple stellar populations following Chabrier initial mass function (see Section 6.1). For consistency, we used the Padova 1994 evolutionary stellar tracks for both the codes, containing the full asymptotic giant branch evolution.

6.1 Initial Mass Function (IMF)

The initial mass function is an important parameter specifying the mass distribution of the stars in the ISM. There are three generic IMFs popularly used in literature:

Salpeter : $\phi(M) \propto M^{-2.35}$ for $0.1 < M < 100$.

Kroupa : $\phi(M) \propto M^{-1.3}$ for $0.1 < M < 0.5$,
 $\phi(M) \propto M^{-2.3}$ for $0.5 < M < 100$.

Chabrier : $\phi(M) \propto M^{-1} \exp \left[\frac{-(\log M - \log m_c)^2}{2\sigma^2} \right]$ for $0.1 < M < 1$,
 $\phi(M) \propto M^{-2.3}$ for $1 < M < 100$.

Here, $\phi(M) = dN(M)/dM \propto M^{-\alpha}$. The normalization is determined such that the integral of $\phi(M)$ between the lower ($0.1 M_\odot$) and upper bounds ($100 M_\odot$) of mass is unity. While the Salpeter (1955) and Kroupa et al. (1993) IMFs follow a simple powerlaw and a broken powerlaw form, respectively, the Chabrier (2003) IMF follows a simple powerlaw above $1 M_\odot$ and a log-normal distribution below $1 M_\odot$, centered on $m_c = 0.08 M_\odot$ with the dispersion in logarithmic mass of 0.69.

Whether the IMF is Universal or varies with environment has been a subject of investigation in many studies (e.g. Cappellari et al. 2013). The results of these studies indicate that the IMF may very well indeed be Universal and described by a power-law with a Salpeter index (2.35) above a few solar masses and log-normal at low masses (see Bastian et al. 2010). This description is very close to the Chabrier-type IMF. This is corroborated by a preliminary analysis that showed that 7 out of 10 BCGs in our sample show a preference for the Chabrier-type IMF. Thus, in order to reduce the number of variables and make the results more comprehensible, for the final simulations we fixed the IMF to Chabrier-type.

6.2 Metallicity

For the metallicity, we assigned three different initial chemical compositions, $Z = 0.008$ ($Z = 0.4 Z_\odot$), 0.02 ($Z = Z_\odot$) and 0.05 ($Z = 2.5 Z_\odot$), to the old and young stellar populations separately,

yielding 9 different combinations. The three metallicities are denoted as Z08, Z02 and Z05, respectively. In what follows, we designate the metallicities of the BCGs with two numbers, “Z1-Z2”, where Z1 is the metallicity of the OSP and Z2 is the metallicity of the YSP. Even though X-ray observations of the 10 BCGs studied in this work indicate sub-solar metallicities at the very centers, where the bulk of the young stars are expected to reside, it is not clear whether X-ray metallicities are a good measure of the stellar metallicities. Hence we left this parameter free.

6.3 Dust: Reddening and Extinction Law

The observed BCG spectra do not reflect the intrinsic SED of the emitting galaxy because of the intervening dust present both in the inter-stellar medium of the Milky Way and also of the BCG. While the spectra may be easily de-reddened to correct for the dust absorption in our Galaxy (Section 3.2), the internal extinction is very hard to determine. The Balmer ratios, such as $H\alpha/H\beta$, in principle, can be used to determine the average reddening value associated with the BCG, $E(B - V)$. However, that line-of-action entails making assumptions on the exact processes producing the Balmer lines, such as whether the line emissions are mostly produced by stars or some other mechanism. A recent study by Fabian et al. (2011) claims a different origin for the $H\alpha$ filaments seen in cool-core BCGs (also see Ogrea et al. 2010). Use of Balmer decrements also depends on the exact physical properties of the emitting media, such as whether the intrinsic Balmer decrements are represented by case-A (optically thin limit) or case-B value (optically thick-limit).

Similarly, there is the issue of which extinction law or curve to invoke to de-fold the observed spectra to get the true spectra. The extinction laws depend on chemical composition and physical properties of the dust grains in the ISM, the metallicity of the ISM, dust geometry etc. There are four main extinction curves used in the literature – the Galactic extinction law (Gal) (Seaton 1979), the Large Magellanic Cloud (LMC) law (Kornneef & Code 1981; Howarth 1983), the Small Magellanic Cloud (SMC) law (Prevot et al. 1984; Bouchet et al. 1985) and the extragalactic extinction (XGal) law (Calzetti et al. 1994). These are shown in Figure 4. The black solid curve represents the spectrum from a simple stellar population with no extinction applied to it. The other curves have the four above-mentioned extinction laws with the same reddening value, $E(B - V)$, applied to them. The Galactic extinction law (dashed red) has the well-known 2175 \AA dust feature visible in it. The LMC and SMC laws are very similar to the Galactic law, although, they differ shortward of $\sim 2500 \text{ \AA}$ and the 2175 \AA feature becomes weaker from the Galactic to the LMC to the SMC. The extragalactic extinction law is visibly distinct from the other three

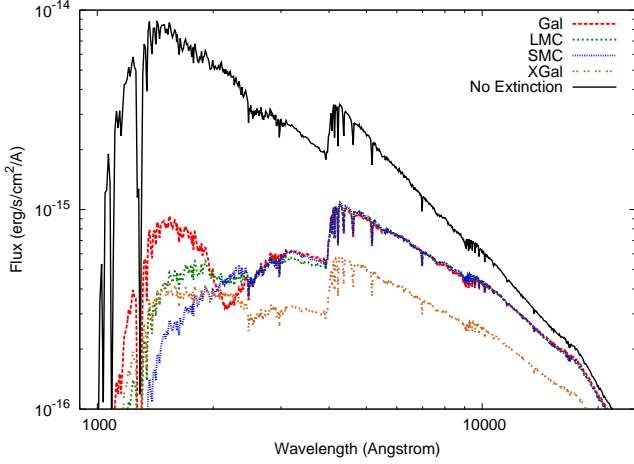


Figure 4. The effect of applying the various extinction laws to a SED obtained using the Kroupa IMF, solar metallicity and an instantaneous burst of $5 \times 10^9 M_{\odot}$ mass stellar population 10^8 yr ago (black curve).

curves in that it is more gray than the other curves but, additionally, it has no evidence of the 2175 Å dust feature.

In this work, instead of fixing the reddening values to ones available in literature, we varied it in the range $0.0 \leq E(B-V) \leq 0.6$ and obtained the most-likely value by marginalizing over other parameters. Similarly, the extinction law was also adopted as a parameter, and we tried the two extreme extinction laws, the Galactic and extragalactic. Both the extinction laws are embedded in the `SYNPHOT` synthetic photometry package distributed as part of the Space Telescope Science Data Analysis System, `STSDAS`. The extinction laws may be applied to any input spectra using the tool `EBMVX`. We used the `GAL1` option to invoke the Galactic extinction law, which uses $R_v = 3.2$ (Seaton 1979), and the `XGAL` option to invoke the extragalactic extinction law, which uses $R_v = 2.43$ (Calzetti et al. 1994).

We note that Calzetti et al. (1994) laid out an empirical formulation of the extragalactic extinction law based on a sample of starburst galaxies. Goudfrooij et al. (1994), on the other hand, investigated 10 elliptical galaxies with dust lanes using surface photometry and found that the most-likely extinction law was close to the Galactic curve, albeit with a lower R_v (between 2.1 and 3.3). The BCGs studied in the paper are elliptical galaxies, although with relatively elevated star formation rates. Letting the extinction law assume one of the two values (Galactic and extragalactic), we find that 4 out of 10 prefer a Galactic extinction law, 2 out of 10 prefer the extragalactic extinction law and 4 out of 10 are compatible with both (see Table 7). Since there is no prior preference for either of the extinction laws, we let this parameter vary between the two types.

6.4 Star Formation Histories

Star formation history (SFH) of a galaxy is a crucial ingredient in stellar population synthesis. Stellar properties, especially, ages and star formation rates, are sensitive to the stellar population models adopted in simulations (e.g. Pforr et al. 2012; Conroy et al. 2010, and references therein).

N-body and semi-analytic simulations of Gao et al. (2004) and De Lucia & Blaizot (2007) showed an early formation of the constituent stars of the BCGs and a late formation of the galaxies themselves, such that most of the stars (> 80%) of the BCGs were al-

Table 7. The posterior mass probabilities for the two adopted extinction laws for the final simulations results.

Cluster	Ext-Laws	
	gal1	xgal
NGC 1275	0.27	0.73
PKS 0745-191	0.70	0.30
Hydra-A	0.49	0.51
ZwCl 3146	0.51	0.49
A 1068	0.65	0.35
A 1795	0.00	1.00
A 1835	0.34	0.66
RXC J1504	0.53	0.47
A 2199	0.51	0.49
A 2597	0.62	0.38

ready in place in different smaller number of progenitor galaxies by $z \sim 3$. The assembly of massive elliptical galaxies and BCGs, in contrast, occurred relatively late ($z < 1$) through dry (dissipationless) mergers of massive hosts with other smaller lower-mass halos.

Subsequent studies, however, indicate a model in which the stellar component in galaxies in cluster centers may have formed as a result of multiple bursts of vigorous star formation at redshifts as recent as $z \sim 2$, and the galaxies thereafter evolving passively (e.g. Eisenhardt et al. 2008; Mei et al. 2009; Mancone et al. 2010). Recently, Brodwin et al. (2013) studied 16 infrared-selected galaxy clusters in the redshift range $1 < z < 1.5$ from the IRAC Shallow Cluster Survey (ISCS) and found $z \sim 1.4$ to be a transition redshift beyond which the cluster galaxies experienced an unquenched era of star formation. A similar study of the ISCS clusters in a wider redshift range $0.3 < z < 1.5$ was conducted by Alberts et al. (2014) using *Herschel* 250 μm imaging with the SPIRE instrument. The study indicates that the cluster galaxies in this redshift range undergo a monotonic increase in star formation and evolve more rapidly than field galaxies. However, the results of Brodwin et al. (2013); Alberts et al. (2014) seem to be driven by low-mass galaxies in both cluster cores and outskirts. High-mass cluster galaxies ($M > 6.3 \times 10^{10} M_{\odot}$) in the centers, such as the BCGs being studied in this paper, have lower specific SFRs than field galaxies but show no strong differential evolution in comparison to the latter (Alberts et al. 2014). This indicates, in compliance with the findings of Peng et al. (2010), that the evolution of the most massive central cluster galaxies is governed by internal physical mechanisms.

Due to limited number of observational constraints, we assume a model with an OSP and YSP, both of which are simple stellar populations. In view of the above studies, it is appropriate that the age of the OSP be allowed to vary between 10 Gyr ($z \sim 1.85$) and 12 Gyr ($z \sim 4$) at 0.5 Gyr intervals. However, our initial results showed that each of the trial values was equally likely. In other words, our data are not sensitive to the OSP age. For the work that follows we fixed the age of the OSP to the formation redshift of $z \sim 3$ (τ_0 11.5 Gyr). Since our BCGs have redshifts in the range [0.02-0.3], light emitted by the stars take a non-negligible amount of time to reach us. So that the OSP has the same formation redshift for all the BCGs, we need to subtract the light-travel time from the age of the Universe at the assumed formation redshift. Except for ZwCl 3146 and A 1835, all the BCGs have a resulting τ_0 age fixed between 9.5 Gyr and 11 Gyr.

For the YSP, we assumed a simple model based on a series of starbursts of the same mass separated by a constant time interval

ranging from 10 Myr to 6 Gyr with a maximum duration of 6 Gyr. Under these assumptions, namely, that (a) the time separation between bursts is the same as the age of the most recent burst and (b) the bursts have the same mass, the number of additional parameters increases only by one and that parameter is the number of bursts, N_{bursts} . Revisiting equation (6),

$$F_i = M_0 S_i^{(o)}(\theta) + M_y \sum_{n=1}^{n=N_{\text{bursts}}} S_{i,n}^{(y)}(\theta) \quad (11)$$

An interesting question that arises is whether, within such a formulation, a model comprising a large number of starbursts occurring periodically is equivalent to one that has a constant star formation rate and thus indistinguishable from it. In Figure 5, we show the two models, continuous (red dashed curves, “CSF”) versus instantaneous or fixed mass (blue solid curves, “FM”) for 10 Myr separation between bursts (top panel) and 1 Myr separation (bottom panel). Both the models have the same total stellar mass. Shown is a comparison between the two models for $N_{\text{bursts}} = 1$, $N_{\text{bursts}} = 4$ and $N_{\text{bursts}} = 50$. While for 1 Myr separation, the two models start coinciding for $N_{\text{bursts}} \geq 1$, for 10 Myr separation the two curves remain qualitatively different at wavelengths ranging from 1000 Å to 4000 Å, by more than the typical measurement uncertainties. This is true also for a large number of bursts. Hence our model with the adopted 10 Myr separation between bursts is such that a multiple burst scenario can *not* be equated to a constant star formation scenario.

The idea behind including a series of stellar bursts is that we would like to determine whether a) there is evidence of any periodicity in star formation and b) if so, whether or not it’s correlated with either the cooling-time of the ICM or AGN activity. Such a correlation would imply that the star formation occurs on a similar time scale as cooling of the ICM or AGN heating. The cooling times within the central few kiloparsec of cool-core clusters can be as short as a few to a few tens of Myrs (Voit et al. 2014) and also the time between AGN outbursts is typically 10^7 yr to 10^8 yr (Fabian et al. 2000; Shabala et al. 2008; Birzan et al. 2012). Hence, we designed our simulations to include a minimum separation of 10 Myr between starbursts. We believe that nobody has explored such a correlation using star formation rates before. While adding a series of periodic bursts in our simulations increases the number of parameters by one, it is an easy feature to include and allows a better understanding of the cooling of the ICM, star formation and AGN-regulated feedback.

7 CONCERNS AND ISSUES

There are some additional concerns, especially that pertaining to elliptical galaxies and cooling-flows, that need to be addressed in the context of modelling stellar populations. These are outlined below. We also present work-arounds to these problems and, although, only approximations, we are confident that they help us assess the parameters more accurately.

7.1 UV-Upturn

The spectrum of some of the elliptical galaxies show an increasing flux with decreasing wavelength at around 2500 Å (e.g. Code & Welch 1979; O’Connell 1999; Atlee et al. 2009). This so-called UV-upturn is believed to be due to hot, extreme horizontal branch stars. The reason as to the existence of such a population of old

Table 8. : A comparison of star formation rates (defined in Section 8.2) with the HST ACS/SBC FUV data point included (third column) and excluded (fourth column).

Cluster	SFR	
	FUV incl.	FUV excl.
Hydra-A	18^{+15}_{-12}	24^{+21}_{-15}
ZwCl 3146	14^{+25}_{-2}	37^{+20}_{-22}
A 1795	21^{+8}_{-10}	20^{+9}_{-10}
A 1835	54^{+19}_{-15}	40^{+14}_{-15}
RXC J1504	67^{+49}_{-36}	66^{+49}_{-37}
A 2597	12^{+11}_{-9}	15^{+13}_{-10}

hot stars is not clear. However, a careful modeling of such stars is required in order to interpret the UV emission from ellipticals and cD galaxies, in particular, that associated with young stars.

A study conducted by Yi et al. (2011) showed that only 5 % of cluster elliptical galaxies (both satellite and BCGs) show the UV-upturn phenomenon. Loubser & Sánchez-Blázquez (2011) studied, on the other hand, only the cluster dominant galaxies and found that there are systematic differences in the UV-colours of BCGs and ordinary ellipticals. To ascertain whether or not the BCGs in the Herschel sample exhibit a UV-upturn, we applied the three criteria listed in Yi et al. (2011) [using the FUV-NUV, FUV-r and NUV-r colours]. We find that of those that have data in all three bands, none fulfill all three criteria, a necessary condition for a galaxy to be classified as a UV-upturn galaxy. Note, the criteria from Yi et al. (2011) are based on a model that comprises only an old stellar population. It is clear from works of Rafferty et al. (2006, 2008); Hicks & Mushotzky (2005); O’Dea et al. (2004, 2008); McNamara et al. (2004); Hansen et al. (1995) that several of the cool-core BCGs are undergoing significant star formation. So, the contribution from the stars causing a UV-upturn to the UV emission is probably even lower than the sample studied by Yi et al. (2011). The work of Donahue et al. (2010), in fact, shows that once the SFR increases beyond $1 M_{\odot} \text{ yr}^{-1}$, the contribution from UV upturn stars from the old stellar population of the BCG, despite being much more massive than the young component, is swamped by that of new stars.

While we can not completely rule out the existence of a UV-upturn in our galaxies, strong cool-core BCGs can not be classified as strong UV-upturn galaxies (since the blue centers are very likely due to young stars). For this work, we do not apply any correction by incorporating stellar population models that contain evolved horizontal branch stars, although such SP models are under construction (H. Jeong, private communication) and in the future it will be interesting to directly explore the effects of evolved branch stars on the SFRs.

7.2 HST ACS/SBC Redleak

For a G-type or later star, the ACS/SBC MAMA detector is known to detect a significant fraction (half or more) of optical and near-UV photons, i.e photons outside the nominal bandpass. Although this effect, termed *redleak*, is incorporated in SYNPHOT, recent investigations carried out by the ACS team have revealed a time and temperature dependence (not taken into account in the sensitivity curves), such that the count rates may increase by 10 % to 20 %. The ACS team is currently working to derive the updated through-

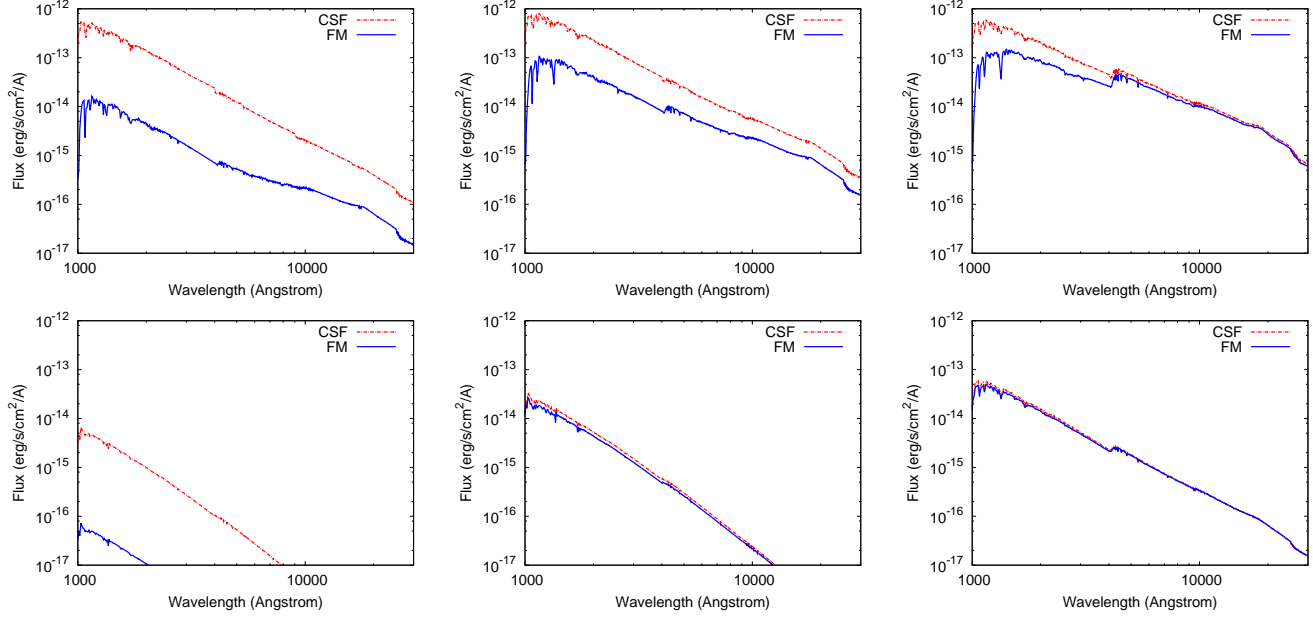


Figure 5. Continuous (red dashed curves, “CSF”) versus instantaneous (blue solid curves, “FM”) star formation models. In the top row panels, the separation between bursts is 10 Myr and in the bottom row panels, the separation between bursts is 1 Myr apart. *Left:* 1 burst, *Middle:* 4 bursts and *Right:* 50 bursts. For 1 Myr separation, the CSF and FM models start coinciding for 4 or greater number of bursts. But for 10 Myr separation, the two curves remain qualitatively different at wavelengths ranging from 1000 Å to 4000 Å by more than the typical measurement uncertainties even when the number of bursts is 50 or higher.

put curves, which will return more accurate estimates (Matt McMaster, private communication). However, since at the time of conducting this work, no correction factors were available, we decided to carry out simulations with and without the HST ACS/SBC FUV data. This way we were able to assess the effect of redleak on the inferred parameters assuming a worst-case scenario. This exercise was possible only for those galaxies that have a GALEX FUV measurement so that there is at least one data point available at FUV wavelengths, needed to constrain the stellar parameters, especially those corresponding to the young stellar component.

In Table 8 we list the star formation rates obtained from including the HST FUV data point and excluding it. If the redleak were a problem, then we would expect the star formation rates inferred from a dataset including the HST ACS/SBC data to be systematically higher than those inferred from a dataset excluding it. There is no such systematic dependence. Aside from the above test, as mentioned in Section 5.1, we also compared the HST FUV to the GALEX FUV fluxes for the same subset of galaxies for which both the data are available and did not find any systematic differences. From this we conclude, that the ACS/SBC redleak is not a major problem and does not affect our results in any way.

7.3 Line Contamination

While codes like STARBURST99 and GALEXEV are able to model stellar and nebular continua, nebular emission lines are not calculated. Hence, ideally it would be nice to model the galaxy SEDs using imaging data devoid of any nebular lines, such as [OII] $\lambda 3727$, H α , H β , [NII] $\lambda 6583$, [OIII] $\lambda 5007$ etc. However, many of the available HST and SDSS data contain line emissions and such a restriction would drastically reduce the number of data points that may be used to obtain a most-likely model. We attempted to remove the contribution from various lines by compiling total line fluxes from the literature, dividing them by the rectangular bandwidth of the

instrument bandpass, and subtracting the resulting line flux-density from the observed flux-density of the images using aperture photometry. In some cases the contributions were too high, like for WFPC2/F439W and WFPC2/F555W observations of PKS 0745-191, the line contributions calculated using the fluxes given in Fabian et al. (1985) are 80 % and 20 % respectively. Such observations were not used. Five of the 10 BCGs needed to be corrected for line emission. These are PKS 0745-191, ZwCl 3146, A 1795, A 1835 and A 2597.

Note that the line fluxes compiled from the literature usually do not correspond to the line emission originating from the entire galaxy but rather to the one-dimensional cross-section of the spectroscopic slits. We made approximate corrections for this shortcoming in the following way. Crawford et al. (1999) is a noteworthy repository of data in this context since they tabulate emission line fluxes of several lines ([OII] $\lambda 3727$, H β , [OIII] $\lambda 5007$, [NII] $\lambda 5199$, H α , [NII] $\lambda 6583$, [SII] $\lambda 6717$, [SII] $\lambda 6731$, [OI] $\lambda 6300$, [OI] $\lambda 6363$) originating from 256 dominant galaxies in 215 clusters. The line fluxes, however, are measured using a 6'' long slit. The H α line fluxes given in Heckman et al. (1989), in contrary, are measured using a narrow-band image and so the integrated line flux density is expected to be higher and more accurate. As an example, the Galactic-extinction corrected H α flux of A 1795 given in Heckman et al. (1989) is about a factor of ten more than that given in Crawford et al. (1999). We used this factor to correct the other line fluxes obtained by Crawford et al. (1999) that are present in the HST (WFPC2/F555W and WFPC2/F702W) and SDSS (*i* and *r*) observations of A 1795. Similarly, by comparing the H α flux estimated by Voit & Donahue (1997) and Heckman et al. (1989), we found that the line fluxes determined by Voit & Donahue (1997) need to be corrected by a factor of 2.5. The various emission lines, the bandpasses in which they lie, along with the references used to make the correction are given in Table 9.

This correction strategy is crude since it may very well be that

Table 9. : The prominent emission lines in the HST and SDSS bands. Given in column 2 are the bandpasses, column 3 are the emission lines and column 3 are the references used to correct for the lines.

Cluster	Bands	Lines	References
PKS 0745	HST/WFPC2 F814W	H α , [NII]	Fabian et al. (1985); Heckman et al. (1989)
ZwCl 3146	HST/WFPC2 F606W SDSS R	[OII], [NII] λ 5199, H β , [OIII] [NII] λ 5199, H β , [OIII]	Crawford et al. (1999) Crawford et al. (1999)
A 1795	HST/WFPC2 F555W, SDSS R HST/WFPC2 F702W, SDSS I	H β , [OIII], [NII] λ 5199 H α , [NII]	Crawford et al. (1999) Heckman et al. (1989); Crawford et al. (1999)
A 1835	HST/WFPC2 F702W SDSS R SDSS I	H β , [OIII], [NII] λ 5199, H α , [NII], [SII] λ 6717, [SII] λ 6731, [OI] λ 6300, [OI] λ 6363 H β , [OIII] H α , [NII]	Crawford et al. (1999) Crawford et al. (1999) Crawford et al. (1999)
A 2597	HST/WFPC2 F450W HST/WFPC2 F702W	[OII], [Ne III] λ 3869, [H η], [H ϵ] + [Ne III] λ 3966, [SII] λ 4069, [H δ], [H γ], [He II] λ 4686 [OI] λ 6300, [OI] λ 6363, [NII], H α , [He I] λ 6678, [SII] λ 6717, [SII] λ 6731, [Ca II] λ 7290, [OII] + [Ca II] λ 7320	Voit & Donahue (1997); Heckman et al. (1989) Voit & Donahue (1997); Heckman et al. (1989)

the lines are not co-spatial, and so we may be over-estimating the correction factors. The difference between the flux-densities with and without the lines are, however, within the uncertainties. Similarly, the best-fit parameters, such as the star formation rates, calculated with and without lines (for NGC 1275: with and without the AGN), are comparable within the uncertainties. The results quoted from hereon refer to measurements after the line correction has been made.

NGC 1275 is a special case. It is host to a bright AGN, 3C 84, with a Seyfert-like spectrum and a radio core-luminosity of order 10^{44} erg s $^{-1}$ (e.g Pedlar et al. 1990). It is possible that the AGN contributes to the UV and optical bands and since we are interested in the flux corresponding only to the stellar component, it is important to assess the AGN fraction and subtract it from the measured flux-densities. In Mittal et al. (2012), we carefully modelled the SED of NGC 1275 from radio to mid-infrared frequencies and obtained simultaneous fits for two dust components and an AGN. Taking the best-fit model at face value, we can use the best-fit parameters to calculate the flux-density due to the AGN. We tabulate in Tables 2–5 both the flux-densities with and without the AGN contribution. As can be seen, the AGN contribution at UV wavelengths is high. The uncertainties assumed for NGC 1275 are conservative and include those due to the AGN contribution. For comparison, the star formation rates with and without the AGN contribution are 78^{+165}_{-60} and 71^{+136}_{-53} .

8 RESULTS

The marginalized posterior probability distributions for the various variables in the parameter space are shown in Figures 8-13 and listed in Table 13. In Figure 14, we show examples of best-fit plots, which were made by fixing the discrete parameters (metallicity, extinction, and YSP age) to their most-likely values given in Table 13 (which are the modes of the individual marginal posteriors) and choosing the most likely M_o and M_y given those choices, which are

the ones that minimize $\chi^2(M_o, M_y, \theta)$ for that choice of θ .⁷ The red and blue curves correspond to the flux contributions from the old and (total) young stellar populations, respectively, and the black curve corresponds to the total spectrum energy distribution (sum of the old and young stellar populations). The green squares correspond to the predicted data and the orange crosses correspond to the observed data. In the following, we discuss the most-likely parameters individually and try to draw generic conclusions.

Since some of the PDFs shown in Figures 8-13 are far from normal distribution, the mean and standard deviation do not convey the usual information about the shape of the distribution. To provide a more robust quantity which is analogous to a $\pm 1\sigma$ error interval, we construct the narrowest 68 % plausible interval, which is the narrowest interval which contains 68% of the area under the posterior PDF, along with the median *within that interval*. Alternative information about the distribution may be captured by the full-width-half-maximum (FWHM) interval, where the probability density at the endpoints is equal to half of the peak value. For comparison, we provide in Table 10 both the 68 % PI and the FWHM interval for the inferred star formation rates, along with the median restricted to each interval. It is encouraging to see that with the exception of NGC 1275, both the 68 % PI and FWHM yield similar median values. For the remainder of the paper, we will use the 68 % PI.

8.1 Young Stellar Population

In Figure 10, we show the posterior mass density function corresponding to the YSP age of the BCGs. The X-axis is the age of the

⁷ Note that this would not generally be guaranteed to give a likely combination of all of the parameters. If the peaks in the posterior are oddly shaped in the discrete parameter space, we could have found that e.g., the most likely metallicity marginalized over τ_y and the most likely τ_y marginalized over metallicity was not a likely combination. But in practice this effect is only pronounced when considering correlations between the masses and other parameters, so as long as we choose the most likely masses for a given likely choice of discrete parameters.

Table 10. The posterior mass probabilities for the two adopted extinction laws for the final simulations results.

Cluster	SFR ($M_{\odot} \text{ yr}^{-1}$) 68 % PI		SFR ($M_{\odot} \text{ yr}^{-1}$) FWHM	
	Median	68% PI interval	Median	FWHM interval
NGC 1275	71	18 – 207	51	24 – 90
PKS 0745-191	24	3 – 64	20	4 – 42
Hydra-A	18	6 – 34	18	7 – 30
ZwCl 3146	14	13 – 40	14	13 – 15
A 1068	8	2 – 21	6	2 – 11
A 1795	21	11 – 28	21	11 – 27
A 1835	54	39 – 73	54	38 – 74
RXC J1504	67	31 – 116	68	31 – 117
A 2199	30	3 – 57	34	0 – 72
A 2597	12	4 – 23	12	5 – 21

youngest starburst and also the separation between multiple starbursts and the Y-axis is the number of starbursts for a given separation. The colourbar represents the probability for a given combination of age and number of outbursts. As an example, in case of Hydra-A, the best fitting combination is given by $\tau_y = 180$ Myr and $N_{\text{bursts}} = 33$. Hence our results show that the “young” stellar component in Hydra-A comprises about 33 starbursts separated roughly by about 0.2 Gyr, the youngest being 0.2 Gyr old and the oldest being 6 Gyr old.

Among all the BCGs, A 2199 seems to be an oddball in that the most-likely model does not call for a “young” stellar component at all. The youngest stellar component is 6 Gyr old. This is in line with the star formation rate estimates derived by Bertola et al. (1986); McNamara et al. (1989); Crawford et al. (1999); Hoffer et al. (2011), the average being 0.2 ± 0.1 (see Table 14), indicating very little ongoing star formation. Our data, however, suggests a complete absence of a young stellar population. One reason this may be is that A 2199 is one of the two BCGs (the other being PKS 0745-191) that has only one data point in the wavelength range [1500 Å to 4000 Å]. So it is possible that with our data we are not able to constrain the YSP as accurately. If we force the age of the YSP to be < 100 Myr, then we obtain $\tau_y = 80$ Myr and a SFR of $\sim 0.3 M_{\odot} \text{ yr}^{-1}$, in consistency with the previous results. The evidence for such a young SP, however, is very small given our data.

Even though A 2199 is the weakest cool-core cluster in the sample with a mass deposition rate of $72^{+2}_{-2} M_{\odot} \text{ yr}^{-1}$ (Hudson et al. 2010), the BCG of A 2199, NGC 6166, harbours a moderately powerful radio source, 3C 338, with symmetric parsec-scale jets (e.g. Gentile et al. 2007, and references therein). Hence it is possible that the BCG experienced an enormous AGN outburst in the past such that the cooling has not yet overcome AGN heating to a degree that is conducive to active star formation.

Four of the 10 BCGs, ZwCl 3146, A 1795, A 1835 seem to favour the youngest stars provided by our simulations. While RXC J1504 is best fitted by a model with a single burst at 10 Myr, the other three seem to prefer multiple bursts with the shortest possible spacing (10 Myr), with ZwCl 3146 and A 1795 going up to the oldest age of 6 Gyr and A 1835 going up to the oldest age of about 3.5 Gyr. In order to investigate whether even younger starbursts might fit the SEDs better, we designed bursts 2 Myr apart for ZwCl 3146 and found that best-fit results were still favouring the youngest stellar population – 2 Myr old – with multiple outbursts going up to 6 Gyr. Hence it seems likely that these four BCGs would be well-fitted by a continuous star formation model.

The median star formation rates inferred from the two models for ZwCl 3146 based on multiple starbursts 10-Myr ($14.4 M_{\odot} \text{ yr}^{-1}$) and 2 Myr ($16 M_{\odot} \text{ yr}^{-1}$) apart are nearly the same. Note that according to the bottom middle panel of Figure 5, a model comprising multiple bursts 1 Myr apart is equivalent to that with a continuous star formation rate for $n_{\text{bursts}} \geq 4$. Similar investigations for RXC J1504 (YSPs with 1 Myr separation although with a limited number of bursts) showed that it might be better-fitted by a continuous star formation model with $N_{\text{bursts}} \gg 1$. Once again, the median star formation rates inferred for the two models are nearly the same. For the present work we give results conducted with 10 Myr spacing and bear in mind that BCGs with a $\chi - 2$ minimum at the upper left corner of the Figures 10 probably favour continuous star formation model. Consideration of a broader range of τ_y and/or simulations with continuous star formation is a promising area for future investigation.

Note that the stellar property solutions inferred from this work are not unique. In principle, the SFH could be such that the star formation rate declines linearly or exponentially or starbursts instead of being instantaneous may be parameterized by a time-decay factor. The SFH chosen in this work is motivated by the notion that cooling of the ICM, star formation and AGN heating may be periodic in nature. However, choosing a different star formation history, or initial mass function (e.g bottom-heavy), may lead to different values of stellar properties. In the future, we will be exploring different forms of star formation histories and their effects on the inferred stellar properties.

8.2 Star Formation Rates

We define the star formation rates as the ratio of the total mass in the young stellar component (mass in one burst multiplied by the number of bursts) to the age of the oldest burst. This quantity is the same as the ratio of the mass in one burst to the age of the most recent burst, since we are assuming bursts for a given BCG to be of the same mass separated by a regular interval of time (see Section 6.4 for more details).

In Figure 11, shown are the posterior probability density function (PDF) for the star formation rates. This is the probability distribution for the mass of the YSP divided by its age, marginalized over all of the other parameters (OSP mass, extinction, etc). A distinct feature visible for some of the BCGs is an asymmetric distribution with a tail extending to the right (towards higher mass) of the peak SFR. This feature is attributed to the fact that the masses of both the OSP and YSP are bounded from below, such that M_o and M_y are both greater than zero. In Table 13, we tabulate the most-likely (mode of the posterior) star formation rates, defined as the peak of the posterior PDFs, along with the narrowest 68 % plausible interval.

It is clear that the star formation rates so derived have a wide range of plausible values. However, the ranges calculated taking into account the various input model parameters are robust. Any additional information, such as priors on the metallicity and/or extinction will help in narrowing down the range of plausible values of the model parameters. As an exercise we fixed the extinction in NGC 1275, PKS 0745 and A 2597 to their best-fit values (the extinction probability density distributions for these three BCGs is the broadest). We list in Table 11 the 68% plausible intervals before and after fixing the extinction. In all three cases, fixing the extinction results in tighter constraints on the SFRs. This highlights the importance of having priors on the internal reddening.

Table 11. Impact on most likely values and plausible intervals of fixing parameters rather than marginalizing. For all three examples, the reddening $E(B-V)$ has been fixed to their best-fit values and we compare the posterior distributions for other parameters to those where we marginalize freely over all extinction values with equal prior weights. Quantities listed are defined in the caption of table 13.

Parameter	NGC 1275		PKS 0745		A 2597	
	$E(B-V)$ free	$E(B-V)$ fixed to 0.12	$E(B-V)$ free	$E(B-V)$ fixed to 0	$E(B-V)$ free	$E(B-V)$ fixed to 0.18
Mo ($10^{11} M_{\odot}$)	1.8 – 4.6	1.6 – 4.5	5.0 – 8.7	6.4 – 8.8	2.4 – 5.0	2.2 – 5.2
My ($10^{10} M_{\odot}$)	6.3 – 16.1	7.3 – 15.3	1.3 – 11.8	0.8 – 6.9	1.1 – 6.4	2.7 – 7.6
My/Mo	0.06 – 0.54	0.06 – 0.52	0.01 – 0.21	0.01 – 0.10	0.01 – 0.19	0.02 – 0.21
Ty (Myr)	110 – 660	80 – 2160	40 – 6000	85 – 5950	20 – 6000	20 – 6000
SFR ($M_{\odot} \text{ yr}^{-1}$)	18 – 207	27 – 72	3 – 64	4 – 23	4 – 23	9 – 19
$E(B-V)$	0.03 – 0.21	...	0.00 – 0.09	...	0.03 – 0.21	...

8.3 Chemical Composition - Metallicity

Since the data used in this study correspond to broadband-imaging rather than detailed spectra, our results may not be very sensitive to the metallicity. Moreover, we include in the model only three candidate metallicities for each stellar population. Therefore we do not quote errorbars in Table 13 but this is not meant to imply precise determination of the metallicities. Rather the reader is encouraged to examine the full posterior distributions. The posterior probabilities shown in Figure 12 (where the first and second strings refers to the OSP and YSP metallicity, respectively) indicate that for the OSP, 4 out of 10 BCGs favour $Z_{08}=0.4 Z_{\odot}$, 3 out of 10 favour $Z_{05}=2.5 Z_{\odot}$, one out of 10 prefers $Z=Z_{\odot}$ and the remaining two do not show a preference for any of the models. For the YSP, 7 out of 10 BCGs favour a low metallicity of $Z_{08}=0.4 Z_{\odot}$.

As far as the OSP is concerned, theoretical models and simulations of Bower et al. (2006); De Lucia & Blaizot (2007); Guo et al. (2011) show that the metallicity distribution of the progenitors peaks in the range $Z = [0.4 - 0.7] Z_{\odot}$, and is pretty much independent of their redshift of accretion. Massive galaxies, such as brightest cluster galaxies, are thought to have formed from smaller progenitors most of whose stellar component was in existence since $z \sim 3$. As these progenitor galaxies evolve and form a higher fraction of stars, so should their metallicity.

The low metallicities, as favoured by 4 out of 10 BCGs in our sample, seem to be in contrast with the results of Loubser et al. (2009); Loubser & Sánchez-Blázquez (2011), where the author(s) studied 49 and 24 BCGs, respectively, in nearby Universe using long-slit optical data and found supersolar metallicities (also see von der Linden et al. 2007). However, the results based on general samples of BCGs, which are usually “red and dead” elliptical galaxies, need not apply to BCGs at the centers of cooling flows that have blue centers. Furthermore, the analysis of Loubser et al. (2009); Loubser & Sánchez-Blázquez (2011) includes only an old stellar population, whereas cool-core BCG spectra essentially need a YSP component to explain the data. Liu et al. (2012), on the other hand, analysed a sample of 120 BCGs using SDSS spectral data of the inner $3''$ region of each BCG and used the SED fitting code *STARLIGHT* to fit their spectra with a model containing SPs of three different ages (young, old and intermediate). Although the average mass-weighted metallicity of their sample is $1.5 Z_{\odot}$, the three cool-core BCGs that overlap between our and their sample – RXC J1504, ZwCl 3146 and A 1835 – have sub-solar metallicities of around $0.5 Z_{\odot}$ (Fengshan Liu, private communication). Our results show that RXC J1504, on the contrary, seems to clearly prefer a supersolar metallicity for the OSP.

Table 12. : The metallicity (within the inner few tens of kpc of the BCGs) inferred from X-ray spectral analysis using either *XMM-Newton* or *Chandra* data. A range of metallicities, where given, corresponds to different models or instruments used, yielding a spread in the average value. (Note PKS 0745 = PKS 0745-191)

Cluster	Z	References
NGC 1275	0.6-0.7	Sanders & Fabian (2007)
PKS 0745	0.4-0.7	Chen et al. (2003); Hicks et al. (2002)
Hydra-A	0.3-0.6	Kirkpatrick et al. (2009); Simionescu et al. (2009)
ZwCl 3146	0.35-0.4	Kausch et al. (2007)
A 1068	0.7-1	Wise et al. (2004)
A 1795	0.4-0.8	Ettori et al. (2002); Gu et al. (2012)
A 1835	0.3-0.4	Schmidt et al. (2001); Majerowicz et al. (2002)
RXC J1504	0.3	Zhang et al. (2012)
A 2199	0.3-0.7	Johnstone et al. (2002)
A 2597	0.5	Morris & Fabian (2005)

The work of Sanderson et al. (2009); Leccardi & Molendi (2008) based on *XMM-Newton* and *Chandra* data of 50 and 20 galaxy clusters, respectively, indicates subsolar metallicities at the centers of galaxy clusters. Dedicated X-ray *XMM-Newton* and *Chandra* observations of cool-core BCGs studied in this work are also consistent with the overall low metallicity result. Table 12 tabulates the metallicities inferred from X-ray observations along with the corresponding references. The central most bins in these observations are a few tens of kiloparsec at most in size and so reflect the metallicities in the ISM of the BCG.

The metallicity inferred from X-ray observations is usually based on the detected iron lines. Other metals need not necessarily have the same ratio to iron as in solar and, moreover, the metallicity of the ISM may not reflect that of the stars. Unfortunately, the metallicity in the BCGs in our sample do not have a measurement based on direct optical stellar features. For A 2597 and NGC 1275, independent measurements lead to further evidence for low metallicities. In the case of A 2597, Voit & Donahue (1997) derived the elemental abundances using the ratio of forbidden-line fluxes to the hydrogen Balmer lines. The derived abundances of Ni II and Si II red and blue emission line doublets led them to conclude that the metallicity in A 2597 is about 0.5 solar, consistent with the result from X-

ray observations (Morris & Fabian 2005). The observations carried out by Voit & Donahue (1997) are possible but hard to achieve even with modern spectrographs since not only is the entire coverage from blue to red ends of the spectrum needed, the spectral resolution needs to be high enough to resolve the NII and SII line doublets. In Mittal et al. (2012), we used optical and infrared line fluxes observed in NGC 1275 and showed that the fluxes predicted from the radiative transfer code CLOUDY better fit the data if the metallicity is assumed to be $\sim 0.6 Z_{\odot}$, once again, consistent with the result from X-ray observations (Sanders & Fabian 2007).

One explanation for low metallicities of the YSP may be embedded in AGN feedback that is essential in cool-core clusters. Khalatyan et al. (2008) used the smooth particle hydrodynamics code to analyse the effect of AGN feedback on the properties of early-type galaxies, including the impact of AGN winds on the chemical abundances of the intergalactic medium (IGM). Their results show that without AGN feedback, metals remain confined to the galactic center whereas with AGN feedback, the IGM goes through metal enrichment via AGN winds that lift the enriched gas from the central regions to outer regions of the halo. The uplifting of the metal enriched gas leads to a strong increase in the metal abundance of the IGM (also see Fabjan et al. 2010) and the effects can be seen as early on as at redshift $z \sim 3$. It seems that it is possible that due to AGN feedback, the ISM in the cool-core BCGs has a low metallicity at all times and therefore the young stars being born from that ISM also have low metallicities.

8.4 Internal Extinction

From Figure 13, it is evident that the internal reddening in the sample of cool-core BCGs is between 0 and 0.25. This is consistent with the conclusions drawn by McDonald et al. (2011), where the authors note a slight deviation of the ratio of UV to $H\alpha$ luminosity from their assumed model. The authors argue that either an intrinsic reddening of $E(B-V) \sim 0.2$ or a top-heavy IMF can account for such a deviation. In McDonald et al. (2012), the authors performed optical spectroscopy of the $H\alpha$ filaments observed in several of the cool-core BCGs (see e.g. Crawford et al. 1999) in a sample of 9 cool-core BCGs. Assuming case B recombination ratios for Balmer lines (an optically thick limit where all photons more energetic than $Ly\alpha$ are re-absorbed and re-emitted through $Ly\alpha$ and longer wavelengths), they were able to determine the internal extinction at more than one location in the BCGs. These locations included the nucleus as well as the filaments. McDonald et al. (2012) found that while the reddening, $E(B-V)$, in the nuclei varies from 0.0 to 0.7, the reddening in the filaments peaked at 0 but had a broad tailed-distribution out to 0.6. These results are in contrast with those of Crawford et al. (1999), who found relatively high reddening in cool core clusters.

We find it very difficult to compare our extinction values to previous works. The reason is two-fold. First, most of the previous studies have either focussed on the nuclei or the specific locations of the filaments (dictated by the spectroscopic slit lengths and positions) associated with the cool-core galaxies. The likely extinction values derived in this paper are based on the flux measurements from the total galaxy. Second, and more importantly, determining internal extinction based on Balmer lines necessarily entails making assumptions on the emission mechanism and the physical conditions of the ISM (such as whether case-A or case-B recombination applies, and whether processes like shock heating and reconnection diffusion are prevalent). In this work, we avoid making assumptions in order to obtain unbiased constraints on the physical

parameters of the stellar populations. This is the reason we subtracted the dominant emission lines from the observed fluxes (see Section 7.3).

9 DISCUSSION

In this section we explore the relation between the properties of the stellar populations in cool-core BCGs, the cooling of the ICM and AGN heating. The most straight-forward derivative from this work that may be compared to the cooling and heating properties is the star formation rate. Note that due to the absence of a young stellar population in A 2199 (Section 8.1), we omit this BCG from all figures that compare the SFRs to cooling and heating properties.

9.1 Link with Cooling Flows

Cooling flows, mass flowing toward the center of galaxy clusters coincident with the brightest cluster galaxy, is expected to manifest itself in the form of star formation. The SFRs in cooling flow clusters have been known to be notoriously low in comparison with the expected mass deposition rate by factors of 10 to 100. We review this result using the SFRs obtained in this work. However, we caution the reader that the correlation plots shown in this section present a lot of scatter, in part due to the fact that the points plotted refer to the median values, in cases, of rather ill-defined posterior distributions.

In the left panel of Figure 6, we plot the star formation rates listed in Table 13 (referred to as “SPS-SFRs” from hereon) against the classical mass deposition rates (CMDR) derived from X-ray observations listed in Table 14. The CMDRs have been re-calculated in some of the cases for a λ CDM cosmology with $H_0 = 71 h_{71} \text{ km s}^{-1} \text{ Mpc}^{-1}$, $\Omega_m = 0.27$ (CMDRs scale with luminosity distance inverse square) and correspond to the mass deposition rate within a radius at which the cooling time of the gas is 7.7 Gyr to 11 Gyr. Based on the detailed density, temperature and metallicity radial profiles of the 5 cool-core clusters belonging to the *HIFLUGCS* sample, which were studied in full extent in Hudson et al. (2010), we find that the CMDRs are nearly constant over radii corresponding to cooling times ranging from ~ 5 Gyr to 11 Gyr (less than 10 % variation). Hence it is not necessary to obtain CMDRs at radii corresponding to exactly the same cooling time. The classical mass deposition rates signify the expected rate at which the intracluster gas is expected to cool in order to maintain hydrostatic equilibrium based purely on a cooling-flow model (e.g. Fabian 1994) and in the absence of any kind of heating (e.g. McNamara & Nulsen 2007). It is typically defined as the ratio of the gas mass encompassed within a radius to the cooling time at that radius. A detailed calculation can be found in Hudson et al. (2010).

The plot shows a weak positive correlation between the classical mass deposition rates and the star formation rates, with a Spearman rank correlation coefficient of 0.43 and a Pearson correlation coefficient of 0.54. A *weak* correlation between the two quantities is not surprising given the scatter. This correlation has a simple interpretation that the star formation in cool-core BCGs is in part or may even largely be due to cooling of the intracluster medium. Rafferty et al. (2006) and O’Dea et al. (2008) obtained similar trends between the two quantities and reached the same conclusion. Also shown in the figure are diagonal lines representing various factors needed to equate the two quantities and we find that the CMDRs are larger than the SPS-SFRs by factors ranging from 4 to 50.

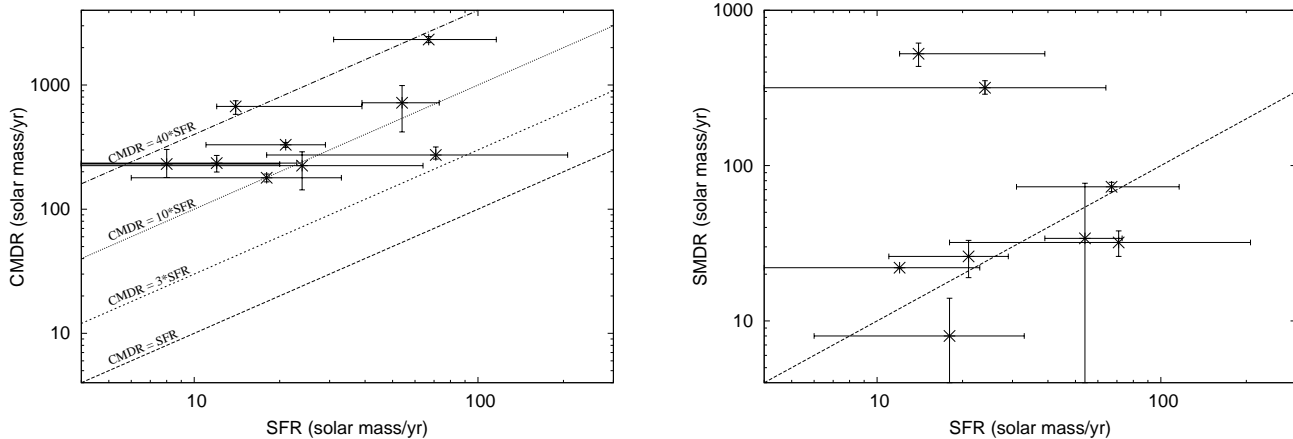


Figure 6. The classical (left) and spectral (right) mass deposition rates (CMDR) calculated from X-ray observations against star formation rates (SFR) derived from the SPS technique. The diagonal line in the right panel represents equality between SMDR and SFR.

This is an expression of the cooling-flow discrepancy (e.g. Hudson et al. 2010), wherein the observed cooling rates (as measured by, for example, star formation rates) are lower than the predicted rates (Birzan et al. 2004; O’Dea et al. 2008). Our results show that the SPS-SFRs instead of being lower than the classical CMDRs by factors of 10 to 100 (Rafferty et al. 2006; O’Dea et al. 2008) are lower by slightly smaller factors (4 to 50). One of the reasons our SFRs may be slightly higher than Rafferty et al. (2006) and O’Dea et al. (2008) is because we chose instantaneous bursts as opposed to continuous star formation models with the former yielding higher masses (left panel of Figure 5).

Similarly, we compared the SPS-SFRs derived in this work to the spectral mass deposition rates (SMDR) derived from X-ray data. SMDRs reflect the actual rate at which the gas is cooling out of the intracluster gas and is obtained by fitting a cooling flow model to the data. The procedure involves technicalities and assumptions that may vary from study to study resulting in a variance in the estimates. In Table 14, we list the SMDRs from *Chandra* and also other observatories, such as *XMM-Newton* and *FUSE*. Since the sensitivity of *Chandra* is lower than that of *XMM-Newton*, the SMDRs obtained from the former are usually considered as upperlimits. However, *XMM-Newton* data for PKS 0745-191 and RXC J1504 result in higher SMDRs than *Chandra* data, which merely reflects the spread in the estimates due to different assumptions.

We plot the SPS-SFRs (this work) against the SMDRs obtained using *XMM-Newton/FUSE* in the right panel of Figure 6. The figure shows that with the exception of ZwCl 3146 and PKS 0745-191 the SPS-SFRs and *XMM-Newton/FUSE* SMDRs are similar. It is interesting that the SPS-SFRs derived in this work are similar to the spectral MDRs, whereas previously, similar to CMDRs, the SFRs have been noted to be lower (by factors up to 10) than the SMDRs. We reckon that the underlying reason for a parity between the SPS-SFRs and SMDRs is that we have obtained a plausible range of star formation rates using a grid of models rather than assuming a single model.

We compiled the star formation rates for the BCGs in our sample from the literature to see how they compare to the SPS-SFRs. The SFRs from the literature are listed in Table 14. The SFRs from Rafferty et al. (2006), compiled in turn from other studies, Hicks & Mushotzky (2005); O’Dea et al. (2010); Donahue et al. (2011) and one of the quoted SFRs in Mittal et al. (2012) are based on

comparison of data with stellar population models. However, these studies usually assume a single stellar population with a fixed IMF and/or metallicity. The internal extinction has been ignored in some of these studies. The SFRs from Edge et al. (2010a); Hoffer et al. (2011) and one of the quoted SFRs from Mittal et al. (2012) are based on MIR or FIR luminosities. Many of the listed SFRs from the literature have small errorbars and are not consistent with each other. We also list the average of the SFRs available in the literature along with the standard deviation. The wide dispersion is clearly visible and comparable to the 68 % plausible intervals for the SPS-SFRs. The reason for such a wide dispersion (on both types of SFRs) is clearly due to a large choice of models available that are capable of fitting the data. We plot the SPS-SFRs against the average SFRs from the literature in left panel of Figure 7. We find that the two types of SFRs are comparable (A 2199 is omitted because the data are consistent with an absence of a YSP).

From the comparison between the SPS-SFRs and SFRs from the literature, we conclude that the star formation rates in BCGs can be well-constrained using the SPS technique yielding a robust range of possible SFRs. In order to obtain a robust range, a complete range of parameters [τ_y , M_o , M_y , IMF, Z , $E(B - V)$] needs to be explored and marginalization techniques need to be employed. To this end, we regard our plausible range of SFRs robust in comparison with the individual SFRs in the literature. In the future, it will be interesting to compare different star formation histories (such as instantaneous versus continuous star formation models) and explore a wider range of OSP and YSP ages.

9.2 Link with AGN Heating

We briefly inspect whether or not the SPS-SFRs have any correlation with the properties of the central radio source in the BCGs. In the generally accepted AGN-regulated feedback framework, the catastrophic cooling of the ICM is simmered down by AGN heating. As the intracluster gas cools, a pressure-driven inward flow is established which serves as fuel for the supermassive black hole residing at the nucleus of the BCG. AGN outbursts, manifested as giant cavities in the X-ray images that overlap with radio jets and lobes, transfer some of the energy back into the ICM via PdV work done by the expanding cavities, and transmitting weak shocks and sound waves into the ICM. Observations of multiple cavities at different radii (e.g. in NGC 1275, Hydra-A, see Fabian et al. 2006;

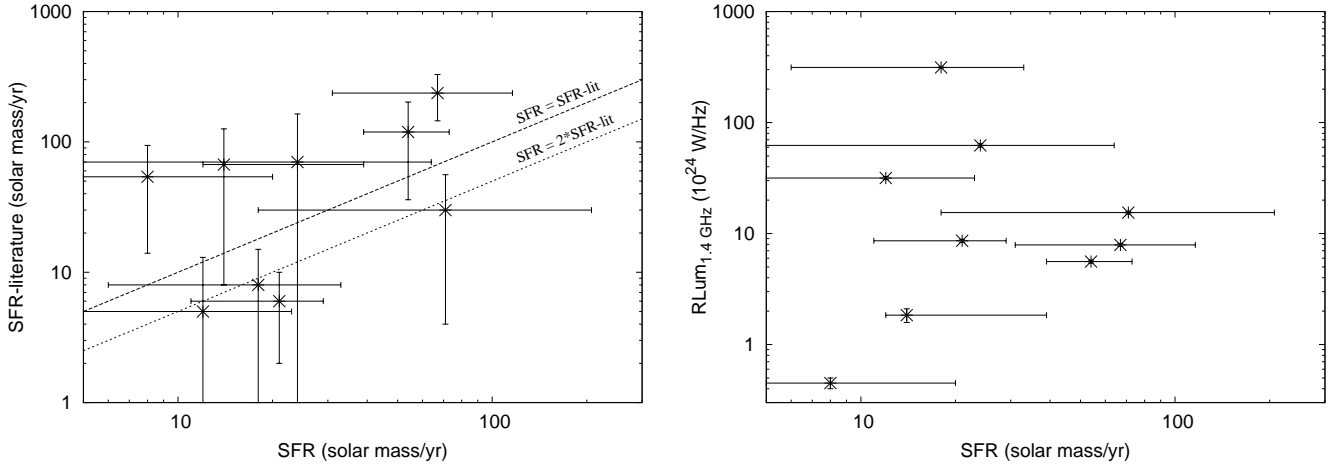


Figure 7. *Left:* The average star formation rates available in the literature versus the star formation rates (SFR) derived from the SPS technique. *Right:* 1.4 GHz radio luminosity against the star formation rates (SFR) derived from the SPS technique. There seems to be a weak anti-correlation between the two quantities.

Birzan et al. 2008, 2012; Rafferty et al. 2006, 2008) indicate that the AGN outbursts are likely periodic. This gives rise to questions as to whether the timescales of AGN activity and cooling are linked. It has been unambiguously shown that there is a correlation between the cooling of the ICM and AGN activity (e.g. Burns 1990; Birzan et al. 2004; Rafferty et al. 2006; Dunn & Fabian 2006; Birzan et al. 2008; Mittal et al. 2009), such that every strong cool-core cluster with central cooling time < 1 Gyr has a radio AGN at the center, the luminosity of which scales as the cluster scale (X-ray mass or luminosity).

As discussed in the previous section, star formation is very likely tied up with cooling, as indicated by a correlation between SPS-SFRs and the classical mass deposition rate. An interesting aspect we explore next is a possible correlation between star formation and AGN activity. Previous studies, such as those by Mittal et al. (2009); Sun (2009), have found a positive correlation between the radio luminosity of the AGN and cooling parameters, like, the CMDR or cooling luminosity (the X-ray luminosity within the cooling region). Such a correlation may be taken as evidence for AGN feedback, such that clusters with higher cooling rates harbour stronger AGN since their ICMs require a greater energy input. As pointed out by Sun (2009), although, such a correlation could also be due to the fact that stronger cool cores are found in more massive clusters which are also able to better confine radio lobes to stop adiabatic expansion and reduce radiative losses. The underlying reason for a positive correlation between the radio luminosity of a centrally located radio source and cooling activity is not yet clear.

In view of the above results, one would expect a positive correlation between the SFR and radio luminosity since the gas inflow both fuels the SFR and the AGN. However, AGN feedback is also believed to quench cooling activity, and hence also the SFR, so one might also expect to find an anti-correlation between the SFR and radio luminosity. In the right panel of Fig. 7, we plot the SPS-SFRs against the 1.4 GHz radio luminosity (compiled from literature that included Birzan et al. 2004; Birzan et al. 2008; Mittal et al. 2009; Govoni et al. 2009, and NED). There is no visible relation between the two quantities. Considering the uncertainty in SFRs and a small number of BCGs in the sample, it is difficult to draw any definite conclusions from this plot. However, given the BCGs in our sample have very different radio morphologies varying from

core dominated (RXC J1504), to compact and diffuse (PKS 0745-191 and A 1835), to small doubles (A 2597 and A 1795), to classic FR-Is (Hydra-A and A 2199), it is difficult to imagine a scenario where the power input in the large lobes is matched to the ongoing star formation. In the future, we will be aiming at expanding the sample so that we may determine statistical correlations between quantities with more surety and robustness.

9.3 Periodicity in Star Formation and its link to Cooling and Heating Network

With the exception of A 2199, all 9 BCGs seem to have had a recent episode of star formation, requiring a young stellar population with $\tau_y < 200$ Myr. Our expectation prior to commencing this work was for all the BCGs in the cool-core sample to show evidence for multiple YSPs since the AGN-regulated feedback entails periodicity in both AGN heating and cooling of the ICM. An important assumption in this argument is that the cool cores were formed long enough ago ($z \sim 1$), that the gas has been cooling for about 7 Gyr – 8 Gyr. This assumption was justified by (Hudson et al. 2010), whose results ruled out a recent formation of cool-cores ($z \lesssim 0.5$) (also see McDonald et al. 2013).

Our results show that 9 out of 10 BCGs indeed require periodic or continuous star formation to explain their broad-band SEDs. An interesting feature for all 9 BCGs is that the star formation seems to have been ongoing since at least 6 Gyr ago. Hence we find that not only cooling but also star formation in cool-core BCGs has been a long-term phenomenon. While ZwCl 3146, A 1795, A 1835 and RXC J1504 seem to require continuous star formation, NGC 1275, PKS 0745, Hydra-A, A 1068 and A 2597 seem to require periodic starbursts with the interval ranging between 20 Myr and 200 Myr. These values correlate well with both the cooling-time of the hot ICM/ISM gas in the inner 5 kpc radius of cool-core BCGs (Voit et al. 2014) and the quiescent phase duration of radio sources in massive galaxies (Shabala et al. 2008). The 5 kpc radius also corresponds to the spatial extent of the youngest stars seen in the form of FUV emission of most BCGs shown in Figure 2. The true star formation history, we note however, is probably much more complex than this simple hypothesis where the stars form periodically at regular intervals with a plausible correlation with the cooling and AGN heating time-scales of the intracluster gas.

In regards to NGC 1275, PKS 0745, Hydra-A, A 1068 and A 2597 seeming to require periodic starbursts, we note that with the exception of A 1068, these BCGs are ones with the highest radio luminosities (see Table 1). From this simple observation, it seems that the periodic starbursts are somehow connected to the synchrotron output of the AGN. It may be that cooling of the ICM in these four BCGs is periodic, such that some of the cooling gas clumps into molecular clouds leading to star formation and some of it fuels the AGN. There is, in fact, observational evidence for multiple cavities in NGC 1275 (Fabian et al. 2006), Hydra A (Wise et al. 2007) and A 2597 (Tremblay et al. 2012b). It is not yet clear whether multiple cavities in cool-core clusters are as a result of continuous jet activity or due to the episodic nature of the AGN on and off state. While our data are not capable of distinguishing between the two scenarios, periodic accretion of cold gas by the supermassive black hole is expected to have a direct impact on the output of the AGN, and can explain the correlation between the existence of periodic starbursts and high radio-luminosity.

As per the results described in Table 13, A 1068 seems to be undergoing regular bursts since 6 Gyr ago at intervals of about 80 Myr. The 68 % plausible range of star formation rate is $2 M_{\odot} \text{ yr}^{-1}$ to $21 M_{\odot} \text{ yr}^{-1}$. This BCG has the lowest 1.4 GHz radio luminosity and so it may be that the AGN is in a quiescent period in the cycle of ICM cooling-AGN heating, which would imply that the AGN activity in cool-core clusters is non-continuous and has a less than 100 % duty-cycle, consistent with the results of Birzan et al. (2012); Donahue et al. (2010).

Lastly, we mention another interesting quantity, which is the ratio of the mass in the young to the mass in the old stellar population, M_y/M_o (column 4 of Table 13). The ratio ranges from a few percent to as high as 30 % suggesting that a significant fraction of stellar mass accumulated since $z \sim 1$.

10 CONCLUSIONS

We have addressed a crucial issue in the domain of cool-core brightest cluster galaxies, namely, how accurately can we determine the star formation rates in these galaxies. This has a direct impact on our understanding of the cooling of the intracluster-medium, star formation and AGN-regulated feedback.

We used broad-band imaging of a sample of 10 strong cool-core BCGs (with central cooling times less than 1 Gyr) and conducted a Bayesian analysis using the technique of stellar population synthesis (SPS) to determine the most likely stellar populations in these BCGs and the properties thereof. Our model consists of an old stellar population and a series of young stellar components. We calculated probability distributions for various model parameters, marginalized over the others. By doing this we were able to obtain 68% plausible intervals for the model parameters, such as the masses in the old and young stellar population, and the star formation rates (SPS-SFRs).

We find that the most-likely SPS-SFRs are factors of 4 to 50 lower than the classical mass deposition rates, the expected rates of mass condensation, inferred from the X-ray data. This range of factors is slightly lower than what was previously thought (10 to 100). The 68% plausible interval on the SFRs is broad, owing to a wide range of models that are capable of fitting the data, and explains the wide dispersion in the star formation rates available in the literature. However, the ranges of possible values, despite being wide, are robust and highlights the strength in Bayesian analyses.

We find that 9 out of 10 BCGs have been experiencing star-

bursts since 6 Gyr ago. While four out of 9 BCGs seem to require continuous star formation rates, 5 out of 9 seem to require periodic star formation on intervals ranging from 20 Myr to 200 Myr. This time scale is similar to the cooling-time of the intracluster gas in the very central (< 5 kpc) regions of BCGs.

ACKNOWLEDGMENTS

We thank the anonymous referee for constructive and detailed feedback. We thank Hyunjin Jeong for the discussion on the UV-upturn phenomenon, Hans Böhringer, Alastair Edge, Christopher O’Dea, Stefi Baum, Megan Donahue, Gabriella Lucia, and Brian McNamara for useful comments and Andy Fabian for a critical feedback. We also thank Fengshan Liu, Shude Mao and Xianmen Meng for their helpful feedback on their metallicity results. Support for program number 12220 was provided by NASA through a grant from the Space Telescope Science Institute, which is operated by the Association of Universities for Research in Astronomy, Inc., under NASA contract NAS5-26555. This publication makes use of data products from the Two Micron All Sky Survey (2MASS), which is a joint project of the University of Massachusetts and the Infrared Processing and Analysis Center/California Institute of Technology, funded by the National Aeronautics and Space Administration and the National Science Foundation. This research has made use of the NASA/IPAC Extragalactic Database (NED) and Galaxy Evolution Explorer (GALEX) data, both of which are operated by the Jet Propulsion Laboratory, California Institute of Technology, under contract with the National Aeronautics and Space Administration, and Ned Wright’s cosmological calculator. STSDAS is a product of the Space Telescope Science Institute, which is operated by AURA for NASA. We thank the `cfitsio` and `wcstools` teams for making available these software for the astronomical community.

REFERENCES

- Ahn C. P., Alexandroff R., Allende Prieto C., Anders F., Anderson S. F., Anderton T., Andrews B. H., Aubourg É., Bailey S., Bastien F. A., SDSS Collaboration 2014, *ApJS*, 211, 17
- Alberts S., Pope A., Brodwin M., Atlee D. W., Lin Y.-T., Dey A., Eisenhardt P. R. M., Gettings D. P., Gonzalez A. H., Jannuzi B. T., Mancone C. L., Moustakas J., Snyder G. F., Stanford S. A., Stern D., Weiner B. J., Zeimann G. R., 2014, *MNRAS*, 437, 437
- Allen S. W., 2000, *MNRAS*, 315, 269
- Allen S. W., Fabian A. C., Johnstone R. M., Arnaud K. A., Nulsen P. E. J., 2001, *MNRAS*, 322, 589
- Atlee D. W., Assef R. J., Kochanek C. S., 2009, *ApJ*, 694, 1539
- Bagchi J., Kapahi V. K., 1994, *Journal of Astrophysics and Astronomy*, 15, 275
- Bastian N., Covey K. R., Meyer M. R., 2010, *ARA&A*, 48, 339
- Benson A. J., et al., 2003, *ApJ*, 599, 38
- Bernardi M., Hyde J. B., Sheth R. K., Miller C. J., Nichol R. C., 2007, *AJ*, 133, 1741
- Bertola F., Gregg M. D., Gunn J. E., Oemler Jr. A., 1986, *ApJ*, 303, 624
- Best P. N., von der Linden A., Kauffmann G., Heckman T. M., Kaiser C. R., 2007, *MNRAS*, 379, 894
- Birzan L., et al., 2004, *ApJ*, 607, 800
- Birzan L., McNamara B. R., Nulsen P. E. J., Carilli C. L., Wise M. W., 2008, *ArXiv e-prints*, 806
- Birzan R., et al., 2012, *MNRAS*, accepted

- Blanton M. R., Schlegel D. J., Strauss M. A., Brinkmann J., Finkbeiner D., Fukugita M., Gunn J. E., Hogg D. W., Ivezić Ž., Knapp G. R., Lupton R. H., Munn J. A., Schneider D. P., Tegmark M., Zehavi I., 2005, *AJ*, 129, 2562
- Bouchet P., Lequeux J., Maurice E., Prevot L., Prevot-Burnichon M. L., 1985, *A&A*, 149, 330
- Bower R. G., et al., 2006, *MNRAS*, 370, 645
- Brodwin M., Stanford S. A., Gonzalez A. H., Zeimann G. R., Snyder G. F., et al., 2013, *ApJ*, 779, 138
- Bruzual G., Charlot S., 2003, *MNRAS*, 344, 1000
- Burbidge E. M., Burbidge G. R., 1965, *ApJ*, 142, 1351
- Burns J. O., 1990, *AJ*, 99, 14
- Calzetti D., Kinney A. L., Storchi-Bergmann T., 1994, *ApJ*, 429, 582
- Cappellari M., McDermid R. M., Alatalo K., Blitz L., Bois M., Bournaud F., Bureau M., Crocker A. F., Davies R. L., Davis T. A., et al., 2013, *MNRAS*, 432, 1862
- Cardelli J. A., Clayton G. C., Mathis J. S., 1989, *ApJ*, 345, 245
- Chabrier G., 2003, *PASP*, 115, 763
- Chen Y., Ikebe Y., Böhringer H., 2003, *A&A*, 407, 41
- Cid Fernandes R., Mateus A., Sodré L., Stasińska G., Gomes J. M., 2005, *MNRAS*, 358, 363
- Code A. D., Welch G. A., 1979, *ApJ*, 228, 95
- Conroy C., White M., Gunn J. E., 2010, *ApJ*, 708, 58
- Crawford C. S., et al., 1999, *MNRAS*, 306, 857
- Croton D. J., Farrar G. R., Norberg P., Colless M., Peacock J. A., Baldry I. K., Baugh C. M., Bland-Hawthorn J., Bridges T., Cannon R., Cole S., Collins C., Couch W., Dalton G., De Propriis R., Driver S. P., et al., 2005, *MNRAS*, 356, 1155
- Croton D. J., Springel V., White S. D. M., De Lucia G., Frenk C. S., Gao L., Jenkins A., Kauffmann G., Navarro J. F., Yoshida N., 2006, *MNRAS*, 365, 11
- De Lucia G., Blaizot J., 2007, *MNRAS*, 375, 2
- Donahue M., Bruch S., Wang E., Voit G. M., Hicks A. K., Haarsma D. B., Croston J. H., Pratt G. W., Pierini D., O'Connell R. W., Böhringer H., 2010, *ApJ*, 715, 881
- Donahue M., de Messières G. E., O'Connell R. W., Voit G. M., Hoffer A., McNamara B. R., Nulsen P. E. J., 2011, *ApJ*, 732, 40
- Dunn R. J. H., Fabian A. C., 2006, *MNRAS*, 373, 959
- Edge A. C., Oonk J. B. R., Mittal R., et al., 2010a, *A&A*, 518, L46
- Edge A. C., Oonk J. B. R., Mittal R., et al., 2010b, *A&A*, 518, L47
- Edwards L. O. V., Hudson M. J., Balogh M. L., Smith R. J., 2007, *MNRAS*, 379, 100
- Egami E., et al., 2006, *ApJ*, 647, 922
- Eisenhardt P. R. M., Brodwin M., Gonzalez A. H., Stanford S. A., Stern D., Barmby P., Brown M. J. I., Dawson K., Dey A., Doi M., Galametz A., Jannuzi B. T., Kochanek C. S., Meyers J., Morokuma T., Moustakas L. A., 2008, *ApJ*, 684, 905
- Ettori S., Fabian A. C., Allen S. W., Johnstone R. M., 2002, *MNRAS*, 331, 635
- Fabian A. C., 1994, *ARA&A*, 32, 277
- Fabian A. C., Arnaud K. A., Nulsen P. E. J., Watson M. G., Stewart G. C., McHardy I., Smith A., Cooke B., Elvis M., Mushotzky R. F., 1985, *MNRAS*, 216, 923
- Fabian A. C., Sanders J. S., Ettori S., Taylor G. B., Allen S. W., Crawford C. S., Iwasawa K., Johnstone R. M., Ogle P. M., 2000, *MNRAS*, 318, L65
- Fabian A. C., Sanders J. S., Taylor G. B., Allen S. W., Crawford C. S., Johnstone R. M., Iwasawa K., 2006, *MNRAS*, 366, 417
- Fabian A. C., Sanders J. S., Williams R. J. R., Lazarian A., Ferland G. J., Johnstone R. M., 2011, *MNRAS*, 417, 172
- Fabjan D., Borgani S., Tornatore L., Saro A., Murante G., Dolag K., 2010, *MNRAS*, 401, 1670
- Fraser-McKelvie A., Brown M. J. I., Pimbblet K. A., 2014, *MNRAS*, 444, L63
- Gao L., Loeb A., Peebles P. J. E., White S. D. M., Jenkins A., 2004, *ApJ*, 614, 17
- Gentile G., Rodríguez C., Taylor G. B., Giovannini G., Allen S. W., Lane W. M., Kassim N. E., 2007, *ApJ*, 659, 225
- Goudfrooij P., de Jong T., Hansen L., Norgaard-Nielsen H. U., 1994, *MNRAS*, 271, 833
- Govoni F., Murgia M., Markevitch M., Feretti L., Giovannini G., Taylor G. B., Carretti E., 2009, *A&A*, 499, 371
- Gu L., Xu H., Gu J., Kawaharada M., Nakazawa K., Qin Z., Wang J., Wang Y., Zhang Z., Makishima K., 2012, *ApJ*, 749, 186
- Guo Q., White S., Boylan-Kolchin M., De Lucia G., Kauffmann G., Lemson G., Li C., Springel V., Weinmann S., 2011, *MNRAS*, 413, 101
- Hansen L., Jorgensen H. E., Norgaard-Nielsen H. U., 1995, *A&A*, 297, 13
- Heavens A. F., Jimenez R., Lahav O., 2000, *MNRAS*, 317, 965
- Heckman T. M., Baum S. A., van Breugel W. J. M., McCarthy P., 1989, *ApJ*, 338, 48
- Hicks A. K., Mushotzky R., 2005, *ApJ*, 635, L9
- Hicks A. K., Wise M. W., Houck J. C., Canizares C. R., 2002, *ApJ*, 580, 763
- Hoffer A. S., Donahue M., Hicks A., Barthelmy R. S., 2012, *ApJS*, 199, 23
- Hoffer H., et al., 2011, in preparation
- Howarth I. D., 1983, *MNRAS*, 203, 301
- Hu E. M., Cowie L. L., Kaaret P., Jenkins E. B., York D. G., Roesler F. L., 1983, *ApJ*, 275, L27
- Hudson D. S., Mittal R., Reiprich T. H., Nulsen P. E. J., Andernach H., Sarazin C. L., 2010, *A&A*, 513, A37+
- Jarosik N., Bennett C. L., Dunkley J., Gold B., Greason M. R., Halpern M., Hill R. S., Hinshaw G., Kogut A., Komatsu E., et al., 2011, *ApJS*, 192, 14
- Jarrett T. H., Chester T., Cutri R., Schneider S., Skrutskie M., Huchra J. P., 2000, *AJ*, 119, 2498
- Johnstone R. M., Allen S. W., Fabian A. C., Sanders J. S., 2002, *MNRAS*, 336, 299
- Kausch W., Gitti M., Erben T., Schindler S., 2007, *A&A*, 471, 31
- Kaviraj S., et al., 2007a, *MNRAS*, 381, L74
- Kaviraj S., et al., 2007b, *ApJS*, 173, 619
- Kennicutt Jr. R. C., 1998, *ARA&A*, 36, 189
- Kennicutt Jr. R. C., Tamblyn P., Congdon C. E., 1994, *ApJ*, 435, 22
- Khalatyan A., Cattaneo A., Schramm M., Gottlöber S., Steinmetz M., Wisotzki L., 2008, *MNRAS*, 387, 13
- Kirkpatrick C. C., Gitti M., Cavagnolo K. W., McNamara B. R., David L. P., Nulsen P. E. J., Wise M. W., 2009, *ApJ*, 707, L69
- Koleva M., Prugniel P., Bouchard A., Wu Y., 2009, *A&A*, 501, 1269
- Koornneef J., Code A. D., 1981, *ApJ*, 247, 860
- Kormendy J., Fisher D. B., Cornell M. E., Bender R., 2009, *ApJS*, 182, 216
- Kroupa P., Tout C. A., Gilmore G., 1993, *MNRAS*, 262, 545
- Larson D., Dunkley J., Hinshaw G., Komatsu E., Nolte M. R., Bennett C. L., Gold B., Halpern M., Hill R. S., et al., 2011, *ApJS*, 192, 16
- Lauer T. R., Faber S. M., Richstone D., Gebhardt K., Tremaine S.,

- Postman M., Dressler A., Aller M. C., Filippenko A. V., Green R., Ho L. C., Kormendy J., Magorrian J., Pinkney J., 2007, *ApJ*, 662, 808
- Leccardi A., Molendi S., 2008, *A&A*, 487, 461
- Leitherer C., Schaerer D., Goldader J. D., González Delgado R. M., Robert C., Kune D. F., de Mello D. F., Devost D., Heckman T. M., 1999, *ApJS*, 123, 3
- Lin Y.-T., Mohr J. J., 2004, *ApJ*, 617, 879
- Liu F. S., Mao S., Meng X. M., 2012, *MNRAS*, 423, 422
- Loubser S. I., Sánchez-Blázquez P., 2011, *MNRAS*, 410, 2679
- Loubser S. I., Sánchez-Blázquez P., Sansom A. E., Soechting I. K., 2009, *MNRAS*, 398, 133
- Majerowicz S., Neumann D. M., Reiprich T. H., 2002, *A&A*, 394, 77
- Mancone C. L., Gonzalez A. H., Brodwin M., Stanford S. A., Eisenhardt P. R. M., Stern D., Jones C., 2010, *ApJ*, 720, 284
- Martin D. C., Fanson J., Schiminovich D., Morrissey P., Friedman P. G., Barlow T. A., Conrow T., Grange R., et al., 2005, *ApJ*, 619, L1
- McDonald M., Benson B. A., Vikhlinin A., Stalder B., Bleem L. E., de Haan T., Lin H. W., Aird K. A., Ashby M. L. N., Bautz M. W., Bayliss M., Bocquet S., Brodwin M., Carlstrom J. E., Chang C. L., et al., 2013, *ApJ*, 774, 23
- McDonald M., Veilleux S., Rupke D. S. N., 2012, *ApJ*, 746, 153
- McDonald M., Veilleux S., Rupke D. S. N., Mushotzky R., Reynolds C., 2011, *ApJ*, 734, 95
- McNamara B. R., et al., 1989, *AJ*, 98, 2018
- McNamara B. R., Nulsen P. E. J., 2007, *ARA&A*, 45, 117
- McNamara B. R., Wise M. W., Murray S. S., 2004, *ApJ*, 601, 173
- Mei S., Holden B. P., Blakeslee J. P., Ford H. C., Franx M., Homier N. L., Illingworth G. D., Jee M. J., Overzier R., Postman M., Rosati P., Van der Wel A., Bartlett J. G., 2009, *ApJ*, 690, 42
- Meurer G. R., Heckman T. M., Calzetti D., 1999, *ApJ*, 521, 64
- Mittal R., et al., 2009, *A&A*, 501, 835
- Mittal R., O’Dea C. P., Ferland G., Oonk J. B. R., Edge A. C., Canning R. E. A., Russell H., Baum S. A., Böhringer H., Combes F., Donahue M., Fabian A. C., Hatch N. A., Hoffer A., Johnstone R., McNamara B. R., Salomé P., Tremblay G., 2011, *MNRAS*, 418, 2386
- Mittal R., Oonk J. B. R., Ferland G. J., Edge A. C., O’Dea C. P., Baum S. A., Whelan J. T., Johnstone R. M., Combes F., Salomé P., Fabian A. C., Tremblay G. R., Donahue M., Russell H., 2012, *MNRAS*, 426, 2957
- Mittaz J. P. D., et al., 2001, *A&A*, 365, L93
- Morris R. G., Fabian A. C., 2005, *MNRAS*, 358, 585
- O’Connell R. W., 1999, *ARA&A*, 37, 603
- Ocvirk P., Pichon C., Lançon A., Thiébaud E., 2006, *MNRAS*, 365, 46
- O’Dea C. P., Baum S. A., Privon G., Noel-Storr J., Quillen A. C., Zufelt N., Park J., Edge A., Russell H., Fabian A. C., Donahue M., Sarazin C. L., McNamara B., Bregman J. N., Egami E., 2008, *ApJ*, 681, 1035
- O’Dea C. P., et al., 2004, *ApJ*, 612, 131
- O’Dea K. P., Quillen A. C., O’Dea C. P., Tremblay G. R., Snios B. T., Baum S. A., Christiansen K., Noel-Storr J., Edge A. C., Donahue M., Voit G. M., 2010, *ApJ*, 719, 1619
- Ogrea G. A., Hatch N. A., Simionescu A., Böhringer H., Brüggén M., Fabian A. C., Werner N., 2010, *MNRAS*, 406, 354
- Pedlar A., Ghataure H. S., Davies R. D., Harrison B. A., Perley R., Crane P. C., Unger S. W., 1990, *MNRAS*, 246, 477
- Peng Y.-j., Lilly S. J., Kovač K., Bolzonella M., Pozzetti L., Renzini A., et al., 2010, *ApJ*, 721, 193
- Peterson J. R., Kahn S. M., Paerels F. B. S., Kaastra J. S., Tamura T., Bleeker J. A. M., Ferrigno C., Jernigan J. G., 2003, *ApJ*, 590, 207
- Pförr J., Maraston C., Tonini C., 2012, *MNRAS*, 422, 3285
- Pipino A., Matteucci F., 2004, *MNRAS*, 347, 968
- Postman M., Lauer T. R., 1995, *ApJ*, 440, 28
- Prevot M. L., Lequeux J., Prevot L., Maurice E., Rocca-Volmerange B., 1984, *A&A*, 132, 389
- Rafferty D., et al., 2008, *ArXiv e-prints*, 802
- Rafferty D. A., et al., 2006, *ApJ*, 652, 216
- Rawle T. D., Edge A. C., Egami E., Rex M., Smith G. P., Altieri B., Fiedler A., Haines C. P., Pereira M. J., Pérez-González P. G., Portouw J., Valtchanov I., Walth G., van der Werf P. P., Zemcov M., 2012, *ApJ*, 747, 29
- Rubin V. C., Oort J. H., Ford Jr. W. K., Peterson C. J., 1977, *ApJ*, 211, 693
- Salomé P., et al., 2006, *A&A*, 454, 437
- Salpeter E. E., 1955, *ApJ*, 121, 161
- Sanders J. S., Fabian A. C., 2007, *MNRAS*, 381, 1381
- Sanderson A. J. R., O’Sullivan E., Ponman T. J., 2009, *MNRAS*, 395, 764
- Scannapieco E., Silk J., Bouwens R., 2005, *ApJ*, 635, L13
- Schmidt R. W., Allen S. W., Fabian A. C., 2001, *MNRAS*, 327, 1057
- Schultz G. V., Wiemer W., 1975, *A&A*, 43, 133
- Seaton M. J., 1979, *MNRAS*, 187, 73P
- Shabala S. S., Ash S. A., Alexander P., Riley J. M., 2008, *ArXiv e-prints*
- Simionescu A., Werner N., Böhringer H., Kaastra J. S., Finoguenov A., Brüggén M., Nulsen P. E. J., 2009, *A&A*, 493, 409
- Siriani M., Jee M. J., Benítez N., Blakeslee J. P., Martel A. R., Meurer G., Clampin M., De Marchi G., Ford H. C., Gilliland R., Hartig G. F., Illingworth G. D., Mack J., McCann W. J., 2005, *PASP*, 117, 1049
- Skrutskie M. F., Cutri R. M., Stiening R., Weinberg M. D., Schneider S., Carpenter J. M., Beichman C., Capps R., et al., 2006, *AJ*, 131, 1163
- Snedden C., Gehrz R. D., Hackwell J. A., York D. G., Snow T. P., 1978, *ApJ*, 223, 168
- Sun M., 2009, *ApJ*, 704, 1586
- Tojeiro R., Heavens A. F., Jimenez R., Panter B., 2007, *MNRAS*, 381, 1252
- Tremblay G. R., O’Dea C. P., Baum S. A., Clarke T. E., Sarazin C. L., et al., 2012a, *ArXiv e-prints*
- Tremblay G. R., O’Dea C. P., Baum S. A., Clarke T. E., Sarazin C. L., et al., 2012b, *ArXiv e-prints*
- Valentijn E. A., Bijleveld W., 1983, *A&A*, 125, 223
- Voit G. M., Donahue M., 1997, *ApJ*, 486, 242
- Voit G. M., Donahue M., Bryan G. L., McDonald M., 2014, *ArXiv e-prints*
- von der Linden A., Best P. N., Kauffmann G., White S. D. M., 2007, *MNRAS*, 379, 867
- Walcher J., Groves B., Budavári T., Dale D., 2011, *Ap&SS*, 331, 1
- Wang J., Overzier R., Kauffmann G., von der Linden A., Kong X., 2010, *MNRAS*, 401, 433
- Wise M. W., McNamara B. R., Murray S. S., 2004, *ApJ*, 601, 184
- Wise M. W., McNamara B. R., Nulsen P. E. J., Houck J. C., David L. P., 2007, *ApJ*, 659, 1153
- Wright E. L., 2006, *PASP*, 118, 1711

Yi S. K., Lee J., Sheen Y.-K., Jeong H., Suh H., Oh K., 2011, ApJS, 195, 22

York D. G., Adelman J., Anderson Jr. J. E., Anderson S. F., Annis J., Bahcall N. A., Bakken J. A., Barkhouser R., Bastian S., Berman E., SDSS Collaboration 2000, AJ, 120, 1579

Zhang Y.-Y., Verdugo M., Klein M., Schneider P., 2012, A&A, 542, A106

Table 13. The most likely physical parameters of the two stellar populations of the BCG sample.

Cluster	M_{\odot} ($10^{11} M_{\odot}$)		M_{\odot} ($10^{10} M_{\odot}$)		M_{\odot}/M_{\odot}		τ_y (Myr)		E(B-V)		SFR ($M_{\odot} \text{ yr}^{-1}$)	
	Median	68% PI	Median	68% PI	Median	68% PI	Youngest	Oldest	Median	68% PI	Median	68% PI
NGC 1275	3.2	1.8 – 4.6	14.2	6.3 – 16.1	0.27	0.06 – 0.54	110	660	0.14	0.03 – 0.21	71	18 – 207
PKS 0745-191	7.0	5.0 – 8.7	6.0	1.3 – 11.8	0.08	0.01 – 0.21	40	6000	0.05	0.00 – 0.09	24	3 – 64
Hydra-A	3.6	2.3 – 4.8	6.0	2.4 – 10.2	0.14	0.02 – 0.33	180	5940	0.06	0.00 – 0.09	18	6 – 34
ZwCl 3146	4.7	4.1 – 5.3	6.0	4.7 – 8.2	0.13	0.08 – 0.18	10	6000	0.00	0.00 – 0.00	14	13 – 40
A 1068	6.9	5.3 – 8.3	2.9	0.4 – 7.1	0.04	0.00 – 0.12	80	6000	0.05	0.00 – 0.09	8	2 – 21
A 1795	8.4	7.4 – 9.4	6.0	1.9 – 10.7	0.06	0.01 – 0.12	10	5860	0.21	0.15 – 0.21	21	11 – 28
A 1835	5.7	4.0 – 7.6	19.7	10.8 – 28.1	0.28	0.07 – 0.51	10	3560	0.15	0.09 – 0.15	54	39 – 73
RXC J1504	7.5	5.6 – 9.3	2.4	0.1 – 7.9	0.03	0.00 – 0.13	10	10	0.00	0.00 – 0.00	67	31 – 116
A 2199	6.2	3.6 – 9.7	9.3	0.1 – 18.8	0.12	0.00 – 0.37	4130	4370	0.09	0.03 – 0.09
A 2597	3.8	2.4 – 5.0	3.5	1.1 – 6.4	0.08	0.01 – 0.19	20	6000	0.14	0.03 – 0.21	12	4 – 23

The most likely physical parameters of the two stellar populations of the BCG sample, defined as the modes of the marginal posterior distributions (shown in figures 12–11) for each of the quantities (probability density functions for τ_y , M_{\odot} , and M_{\odot} and probability mass function for metallicity and extinction). The columns are: (1) cluster, (2) mass of the old stellar population (peak and the 68% plausible interval), (3) the total mass of the young stellar population (peak and the 68% plausible interval), (4) the ratio of the total mass in the YSP to that in the OSP, (5) the youngest and the oldest YSP age (6) the internal extinction and (7) the star formation rate (peak and the 68% plausible interval); defined as the ratio of mass of a single burst to the age of the most recent burst. “PI 68%” corresponds to the endpoints of the narrowest 68% plausible interval constructed from the marginal posterior (which is shown shaded on the corresponding posterior plot). The SED for A 2199 does not seem to require a YSP at all. Therefore there is no “ongoing” star formation rate in A 2199. The best-fit model for RXC J1504 comprises a single YSP burst.

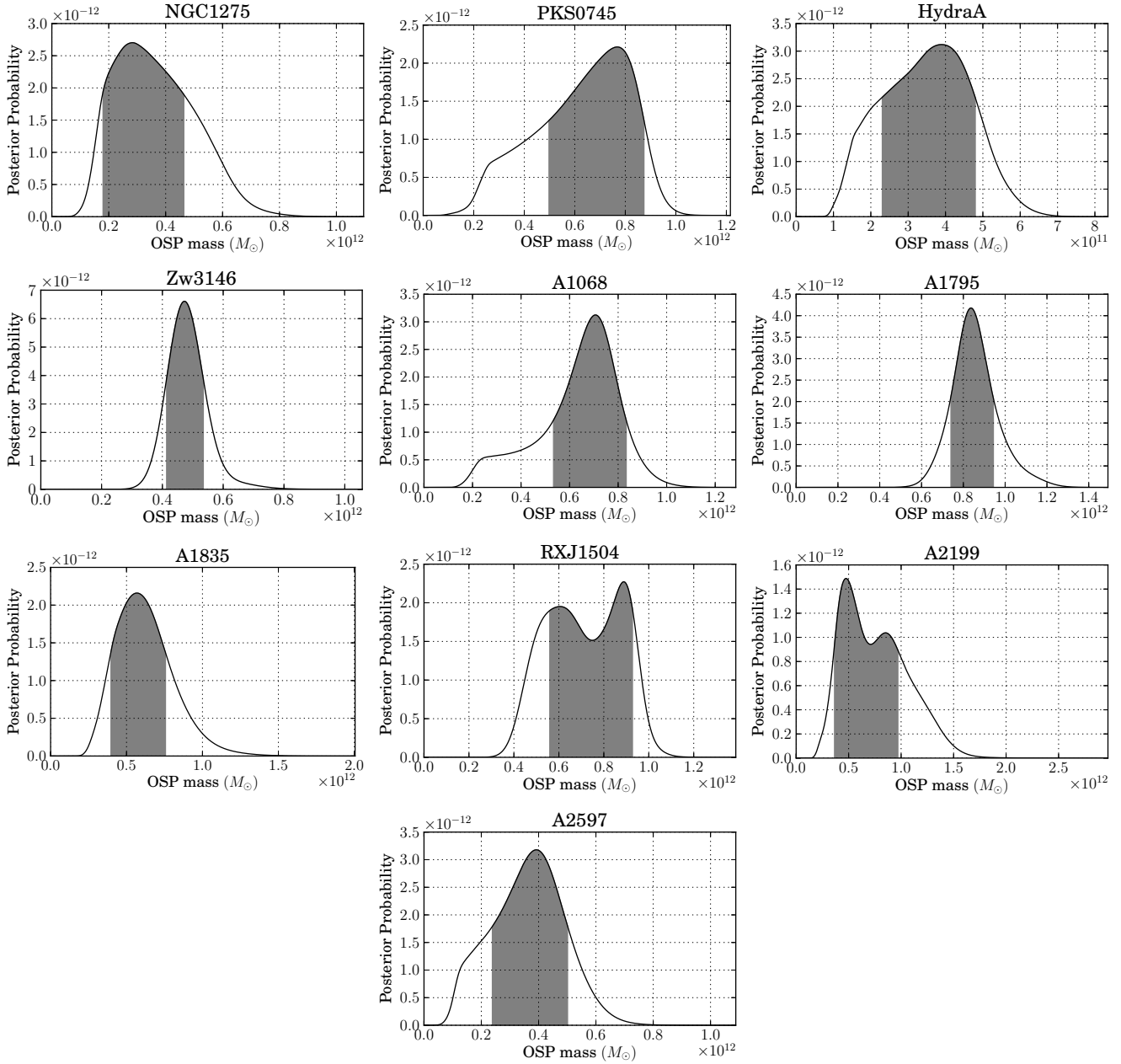


Figure 8. Posterior probability density functions for the mass of the old stellar population, M_o , after marginalizing over other model parameters (metallicity, extinction, YSP age and YSP mass). The joint prior PDF used for M_o and M_y was uniform with the constraint that $M_o > M_y$. Since the best fit YSP masses for most models were much lower than the corresponding OSP masses, this can be thought of effectively as a uniform prior on M_o . The shading indicates the narrowest 68% plausible interval for M_o .

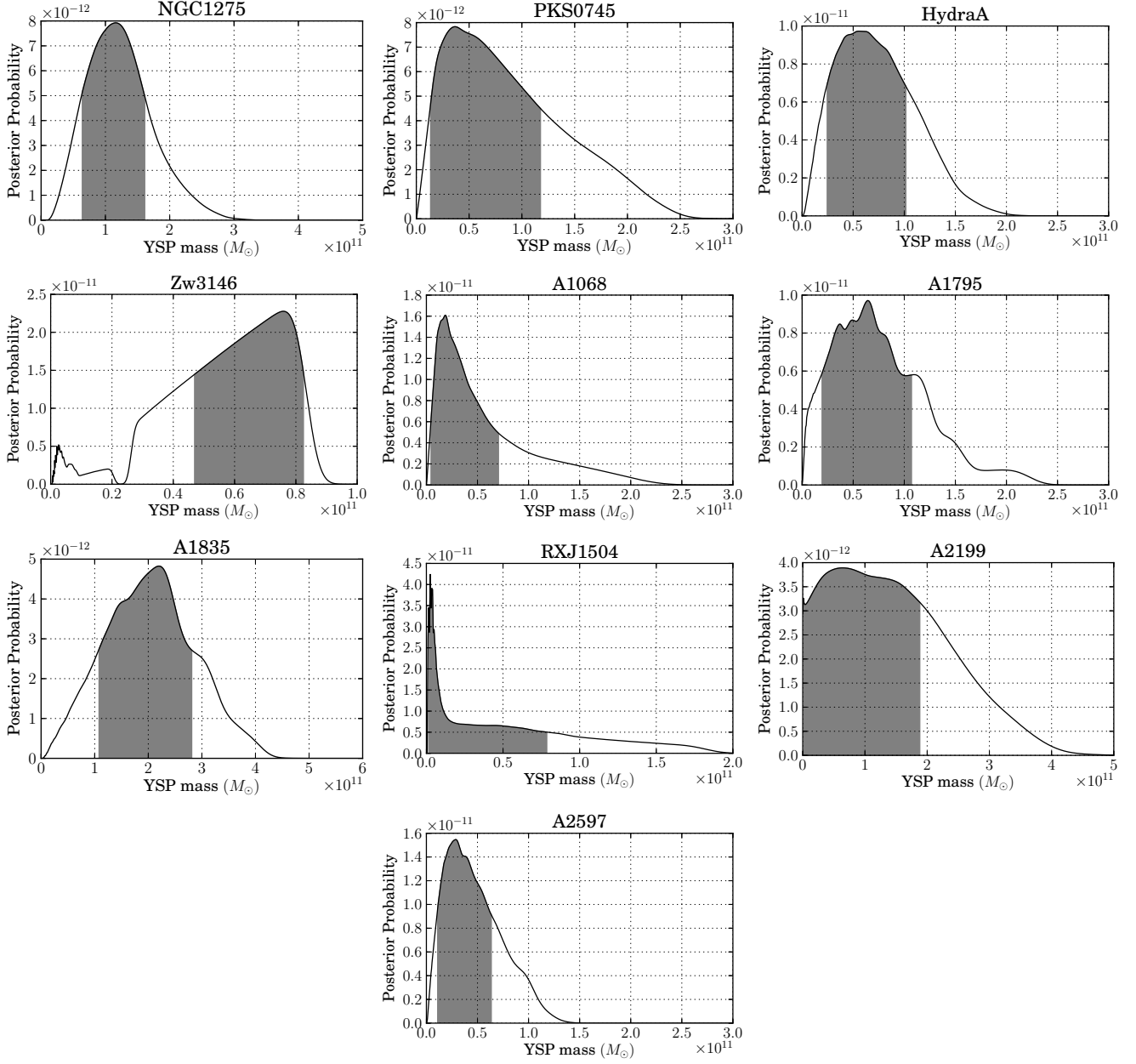


Figure 9. Posterior probability density distributions for the mass of the young stellar population, M_y , after marginalizing over other model parameters (metallicity, extinction, YSP age and OSP mass). The joint prior PDF used for M_o and M_y was uniform with the constraint that $M_o > M_y$. Since the best fit YSP masses for most models were much lower than the corresponding OSP masses, this can be thought of effectively as a uniform prior on M_y . The shading indicates the narrowest 68% plausible interval for M_o . Note that some of the multimodality in the posterior pdf for M_y is likely not a “real” feature, but an artifact of the discrete sampling of τ_y , which is correlated with M_y in the joint posterior distribution.

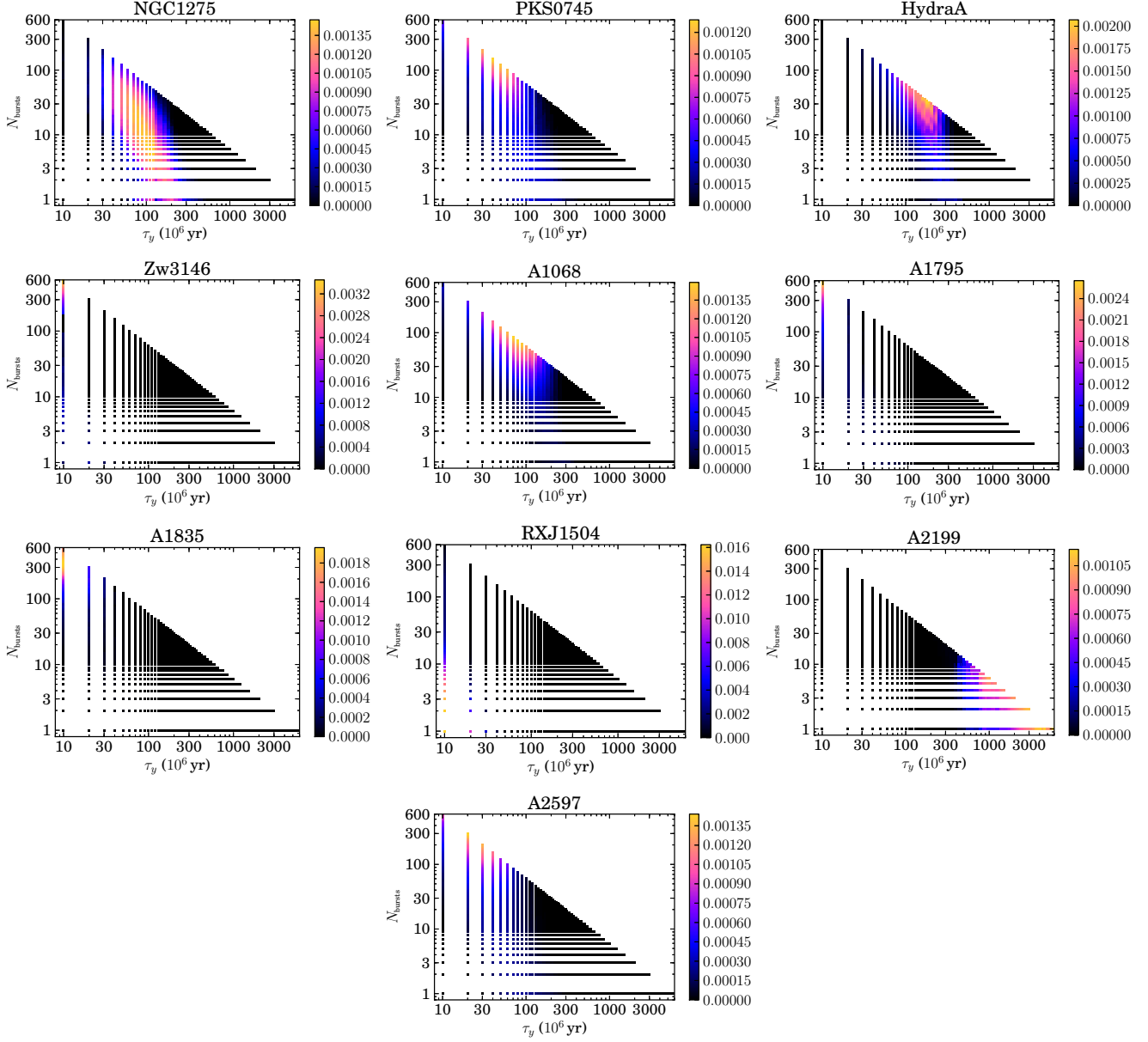


Figure 10. Posterior probability distributions for the age of the YSP, after marginalizing over other model parameters (metallicity, extinction, OSP and YSP). The X-axis represents the age of the most recent starburst and also the separation between multiple starbursts and the Y-axis represents the number of outbursts for a given separation. Each of the combinations of these two parameters was assigned equal prior probability; The colourbar represents the posterior probability for a given combination of age and number of outbursts.

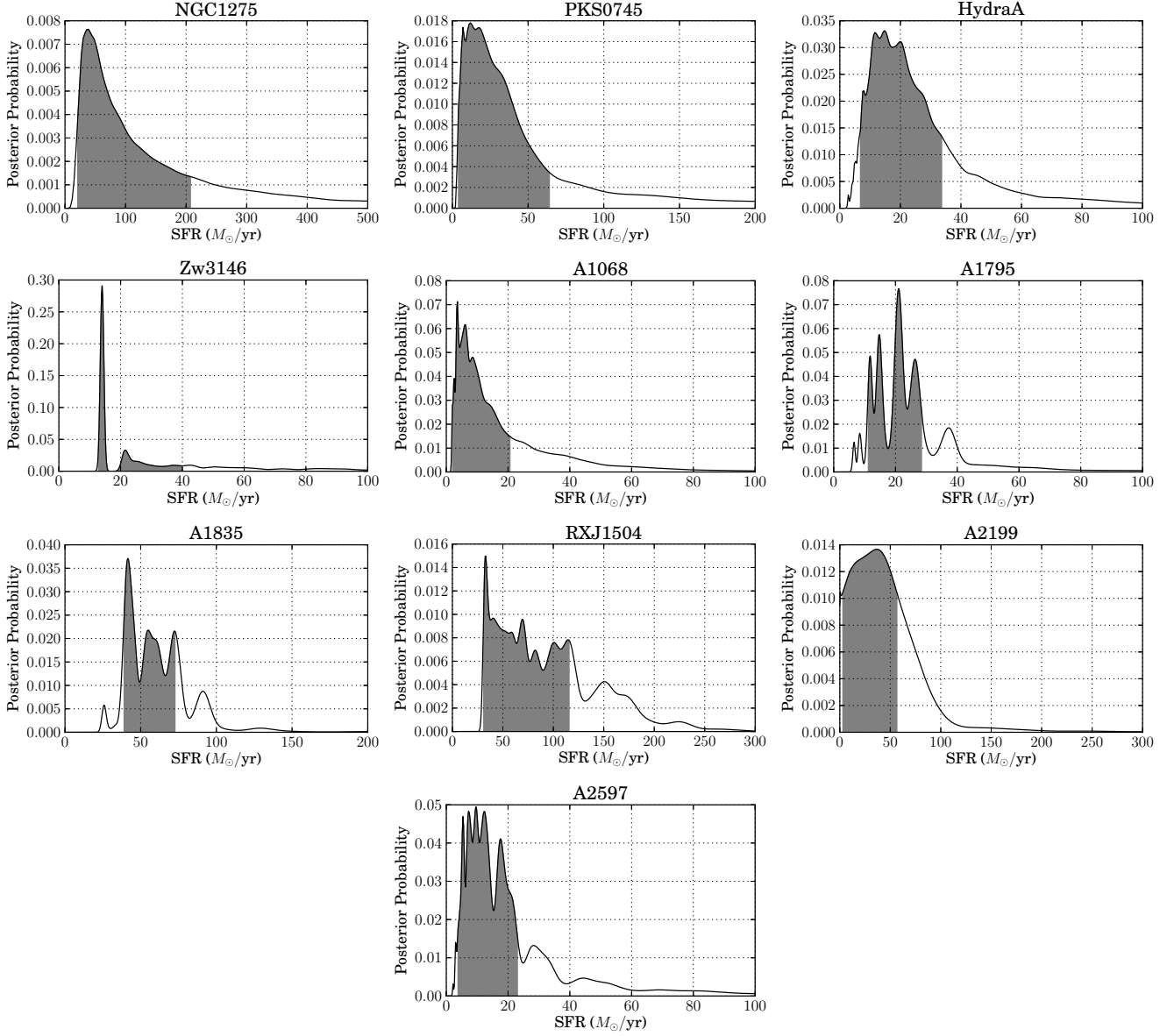


Figure 11. The posterior probability density distributions for the star formation rates, constructed from the joint posterior probability distribution for the mass and age of the young stellar population, after marginalizing over other model parameters (metallicity, extinction, and OSP mass). The SFR is the total mass divided by the age of the oldest burst, or equivalently the mass in each burst divided by the time interval between them. Note that some of the multimodality in the posterior pdf for the SFR is likely not a “real” feature, but an artifact of the discrete sampling of τ_y .

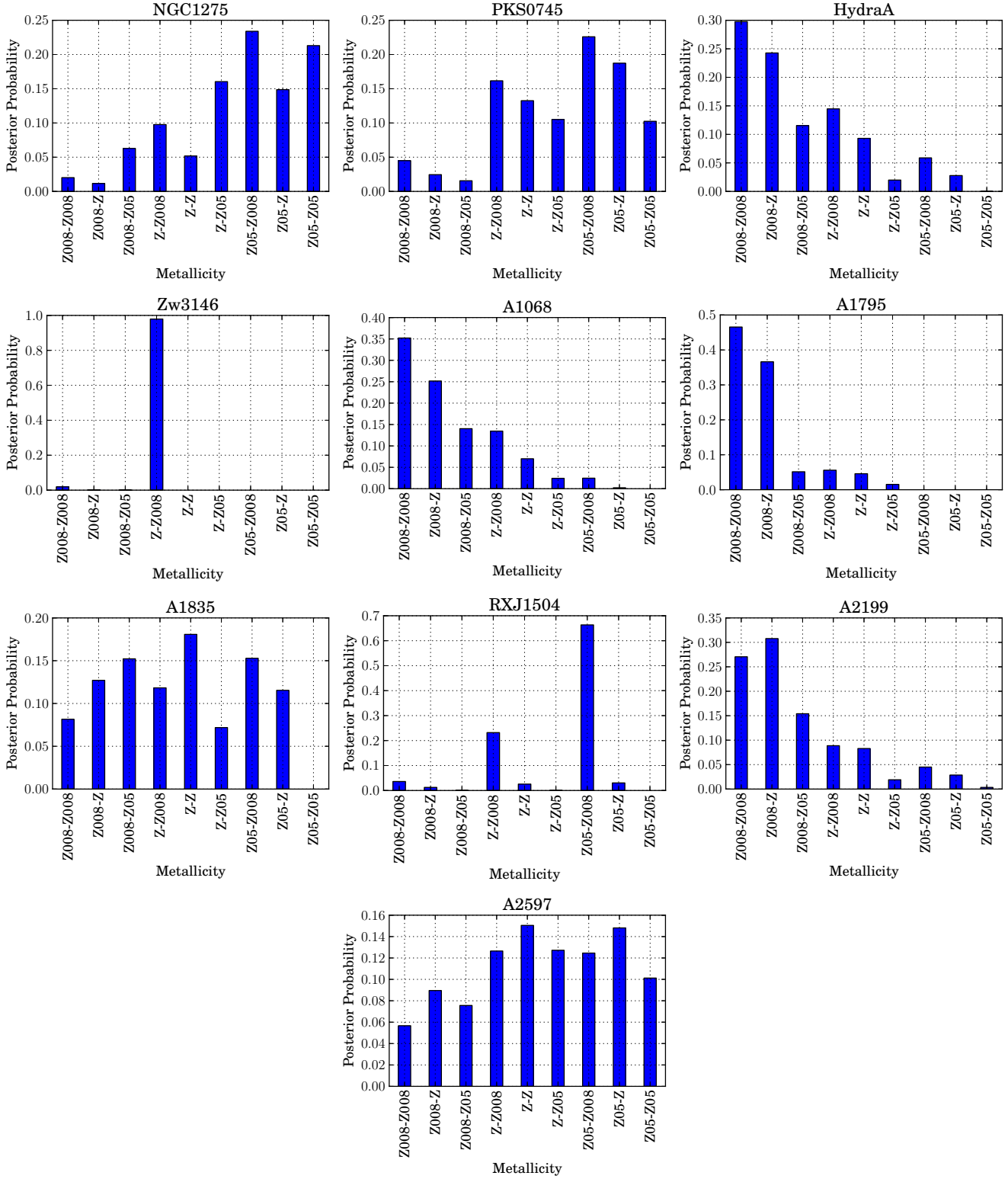


Figure 12. The posterior probability distributions for the metallicity of the young and old stellar populations, marginalized over the other model parameters (extinction, YSP age, OSP and YSP masses). The labels refer to the metallicity values for the old and young stellar populations, respectively. “Z008” means $Z = 0.008$, “Z” means $Z = 0.02 = Z_{\odot}$, and “Z05” means $Z = 0.05$. The assumed prior probabilities were equal for each of the nine combinations.

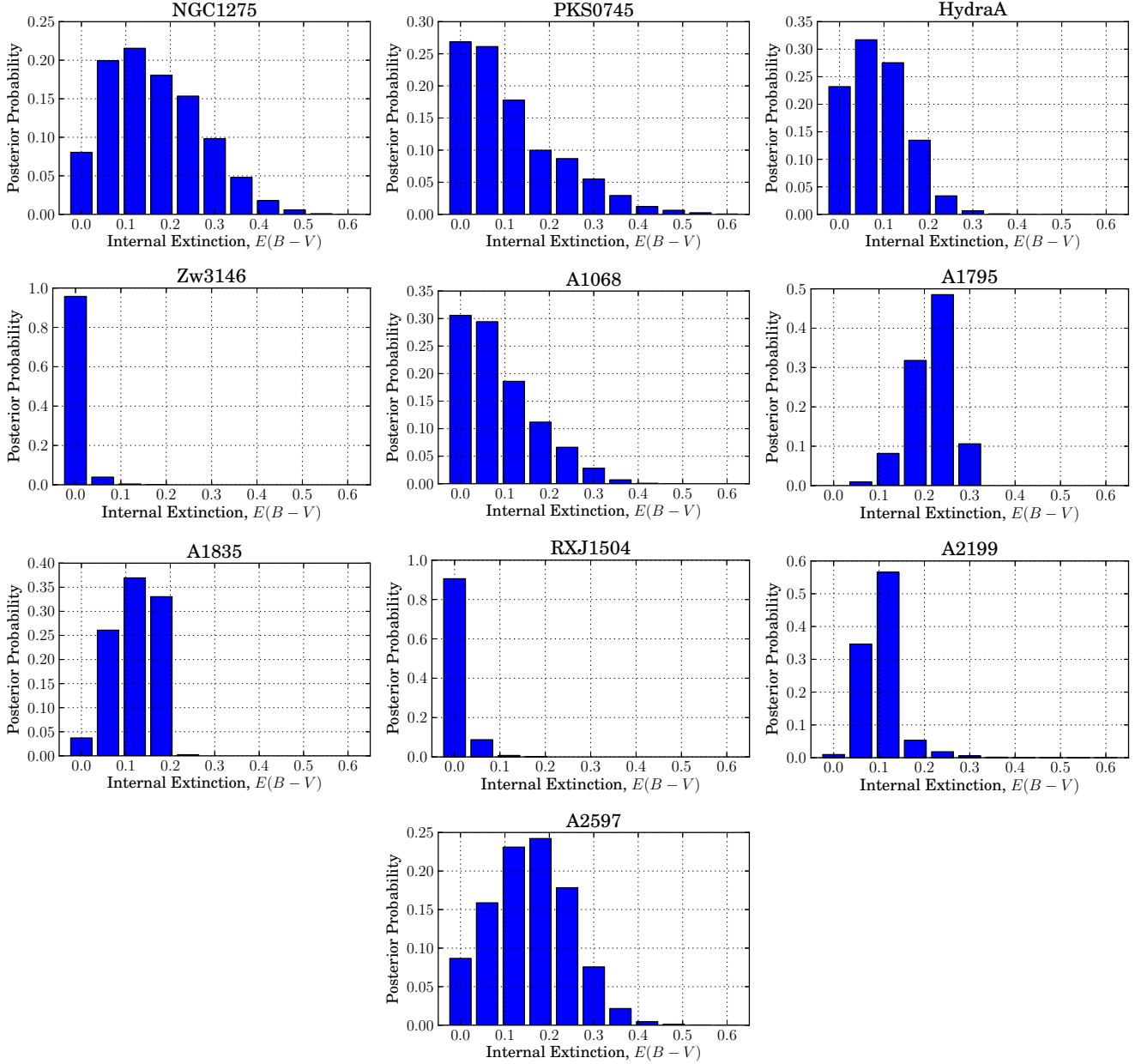


Figure 13. The posterior probability distributions for the internal extinction, $E(B - V)$, after marginalizing over other model parameters (metallicity, YSP age, OSP and YSP masses). The prior probability distribution used for $E(B - V)$ was uniform.

Table 14. A comparison of X-ray mass deposition rates and star formation rates.

Cluster	"SPS-SFR $M_{\odot} \text{ yr}^{-1} h_{71}^{-2}$	CMDR <i>Chandra</i> $M_{\odot} \text{ yr}^{-1} h_{71}^{-2}$	SMDR <i>Chandra</i> $M_{\odot} \text{ yr}^{-1}$	SMDR <i>XMM/USE</i> $M_{\odot} \text{ yr}^{-1}$	Star Formation Rates (literature) $M_{\odot} \text{ yr}^{-1} h_{71}^{-2}$	Average SFR (Literature) $M_{\odot} \text{ yr}^{-1} h_{71}^{-2}$
NGC1275	71^{+36}_{-53}	273^{+44}_{-20} (d)	54^{+48}_{-18} (f)	32^{+6}_{-6} (e)	$2.3^{+0.2}_{-0.2}$ (e), $15.5^{+5.2}_{-5.2}$ (e), 37 (e), 24^{+1}_{-1} (i), 27 (i), 70^{+7}_{-7} (n)	30 ± 23
PKS0745	24^{+40}_{-21}	224^{+66}_{-81} (c)	170^{+90}_{-90} (e)	317^{+35}_{-29} (g)	$16.9^{+5.6}_{-5.6}$ (e), 129^{+7}_{-7} (g), 237^{+13}_{-13} (g), 17 (k), 11 (m), $8.5^{+0.9}_{-0.9}$ (n)	70 ± 94
HydraA	18^{+15}_{-12}	179^{+13}_{-13} (b)	16^{+5}_{-5} (e)	8^{+6}_{-4} (g)	≤ 0.5 (e), ~ 16 (e), $9.5^{+0.2}_{-0.2}$ (g), $17.5^{+0.4}_{-0.4}$ (g), 4.3 (m), $2.1^{+0.2}_{-0.2}$ (n)	8 ± 7
ZwCl3146	14^{+25}_{-7}	673^{+74}_{-93} (c)	590^{+190}_{-170} (e)	525^{+90}_{-90} (g)	10.7 (e), ≤ 110 (e), 91^{+4}_{-4} (g), 168^{+8}_{-8} (g), 44^{+14}_{-14} (j), 12.4 (l), $31.3^{+3.1}_{-3.1}$ (n)	67 ± 59
A1068	8^{+12}_{-10}	231^{+72}_{-51} (c)	≤ 48 (e)	...	18.1 (e), 28^{+12}_{-12} (e), 46^{+21}_{-21} (e), 60^{+20}_{-20} (j), 188 (k), 100 (m), $119.4^{+11.9}_{-11.9}$ (n)	80 ± 60
A1795	21^{+8}_{-15}	330^{+15}_{-15} (b)	8^{+13}_{-7} (e)	26^{+7}_{-7} (e)	$1^{+0.1}_{-0.1}$ (e), 1.1 (e), $2.1^{+0.9}_{-0.9}$ (e), 6.3 (e), 23.2 (e), $9.1^{+0.2}_{-0.2}$ (g), $16.7^{+0.4}_{-0.4}$ (g), 2.3 (m)	8 ± 8
A1835	54^{+19}_{-36}	720^{+270}_{-301} (c)	100^{+100}_{-70} (h)	34^{+43}_{-34} (g)	48.9 (e), 79 (e), 79.5 (e), 140^{+40}_{-40} (e), 123^{+5}_{-5} (g), 226^{+9}_{-9} (g), 11.7 (l), 270 (m), $97.2^{+9.7}_{-9.7}$ (n)	119 ± 83
RXC J1504	67^{+49}_{-27}	2327^{+130}_{-130} (b)	≤ 7.4 (b)	73 (o)	136 (o), 262 (o), 314 (o)	237 ± 92
A2199	...	72^{+12}_{-1} (b)	2^{+1}_{-1} (b)	...	$0.10^{+0.03}_{-0.03}$ (e), 0.10 (e), $0.4^{+0.1}_{-0.1}$ (n)	0.2 ± 0.1
A2597	12^{+11}_{-9}	235^{+36}_{-36} (b)	30^{+30}_{-20} (b)	22 (e)	$2.3^{+1.3}_{-1.3}$ (e), 6.4 (e), 22.3 (e), 2^{+1}_{-1} (j), 5.4 (m), $1.4^{+0.2}_{-0.2}$ (n)	5 ± 8

a, this work; b, Hudson et al. (2010), unpublished; c, Allen (2000); d, Allen et al. (2001); e, Rafferty et al. (2006), and references therein; f, Birzan et al. (2004); g, Hicks et al. (2005); h, Egami et al. (2006); i, Mittal et al. (2012); j, Edge et al. (2010); k, O'Dea et al. (2008); l, O'Dea et al. (2010); m, Donahue et al. (2011); n, Hoffer et al. (2012); o, Ogarean et al. (2010).

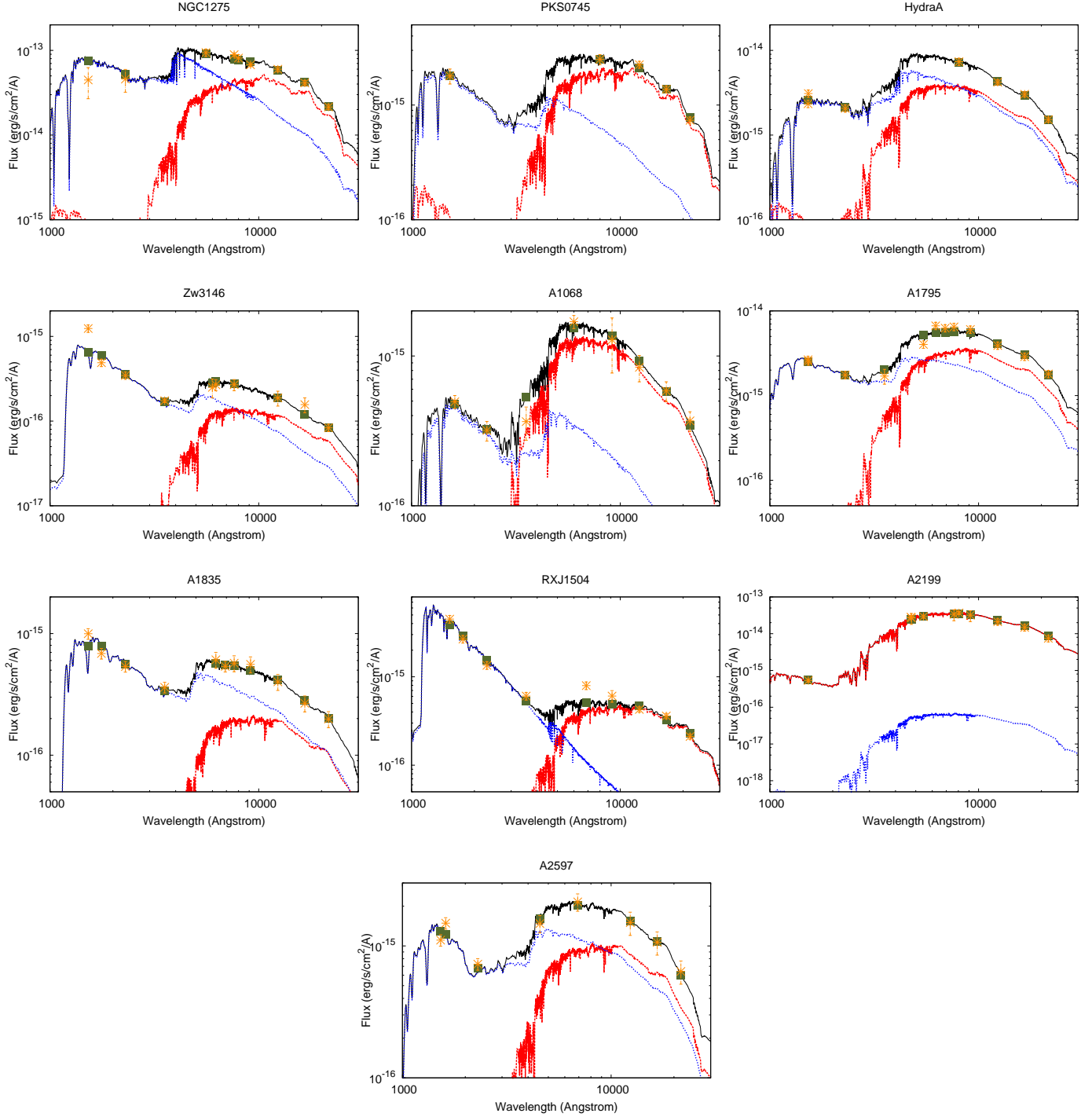


Figure 14. Example best-fit plots shown by fixing all the discrete parameters (metallicity, extinction, and YSP age) to their most-likely values (the modes of their individual marginal posteriors) and then choosing the most likely YSP and OSP masses given that choice (which occurs at the minimum χ^2). The red and blue curves correspond to the flux contributions from the old and (total) young stellar populations, respectively, and the black curve corresponds to the total spectrum energy distribution (sum of the old and young stellar populations). The green squares correspond to the predicted data and the orange crosses correspond to the observed data.